

Detailed analysis of excited state systematics in a lattice QCD calculation of g_A

Jinchen He,^{1,2} David A. Brantley,³ Chia Cheng Chang (張家丞),^{4,5,2} Ivan Chernyshev,^{2,6}
 Dean Howarth,^{3,5} Christopher Körber,^{7,5} Aaron S. Meyer,^{2,5} Henry Monge-Camacho,^{8,9}
 Enrico Rinaldi,^{10,11,4} Chris Bouchard,¹² M.A. Clark,¹³ Arjun Singh Gambhir,^{14,5}
 Christopher J. Monahan,^{15,16} Amy Nicholson,^{8,5} Pavlos Vranas,^{3,5} and André Walker-Loud^{5,3,2}
 (CalLat Collaboration)*

¹*Department of Physics, University of Chinese Academy of Sciences, Beijing, 100049, P. R. China*

²*Department of Physics, University of California, Berkeley, CA 94720, USA*

³*Physics Division, Lawrence Livermore National Laboratory, Livermore, CA 94550, USA*

⁴*Interdisciplinary Theoretical and Mathematical Sciences Program*

(iTHEMS), RIKEN, 2-1 Hirosawa, Wako, Saitama 351-0198, Japan

⁵*Nuclear Science Division, Lawrence Berkeley National Laboratory, Berkeley, CA 94720, USA*

⁶*Department of Physics, University of Washington, Seattle, WA 98195, USA*

⁷*Institut für Theoretische Physik II, Ruhr-Universität Bochum, D-44780 Bochum, Germany*

⁸*Department of Physics and Astronomy, University of North Carolina, Chapel Hill, NC 27516-3255, USA*

⁹*Escuela de Física, Universidad de Costa Rica, San José, San Pedro, 11501, Costa Rica*

¹⁰*Physics Department, University of Michigan, Ann Arbor, MI 48109, USA*

¹¹*Theoretical Quantum Physics Laboratory, RIKEN, 2-1 Hirosawa, Wako, Saitama 351-0198, Japan*

¹²*School of Physics and Astronomy, University of Glasgow, Glasgow G12 8QQ, UK*

¹³*NVIDIA Corporation, 2701 San Tomas Expressway, Santa Clara, CA 95050, USA*

¹⁴*Design Physics Division, Lawrence Livermore National Laboratory, Livermore, CA 94550, USA*

¹⁵*Department of Physics, The College of William & Mary, Williamsburg, VA 23187, USA*

¹⁶*Theory Center, Thomas Jefferson National Accelerator Facility, Newport News, VA 23606, USA*

(Dated: April 8, 2021)

Excited state contamination remains one of the most challenging sources of systematic uncertainty to control in lattice QCD calculations of nucleon matrix elements and form factors. Most lattice QCD collaborations advocate for the use of high-statistics calculations at large time-separations ($t_{\text{sep}} \gtrsim 1$ fm) in order to combat the signal-to-noise degradation. In this work we demonstrate that, for the nucleon axial charge, the alternative strategy of utilizing a large number of relatively low-statistics calculations at short to medium time separations ($0.2 \lesssim t_{\text{sep}} \lesssim 1$ fm), combined with a multi-state analysis, provides a more robust and economical method of quantifying and controlling the excited state systematic uncertainty, including correlated late-time fluctuations that may bias the ground state. We also demonstrate that two classes of excited states largely cancel, leaving the third class, the transition matrix elements, as the dominant source of excited state contamination. On an $a \approx 0.09$ fm, $m_\pi \approx 310$ MeV ensemble, we observe the expected exponential suppression of excited state contamination in the Feynman-Hellmann correlation function relative to the standard three-point function; the excited states of the regular three-point function reduce to the 1% level for $t_{\text{sep}} > 2$ fm while for the Feynman-Hellmann correlation function, they are suppressed to 1% at $t_{\text{sep}} \approx 1$ fm. Independent analyses of the three-point and Feynman-Hellmann correlators yields consistent results for the ground state. However, a combined analysis allows for a more detailed and robust understanding of the excited state contamination, improving the demonstration that the ground state parameters are stable against variations in the excited state model, the number of excited states, and the truncation of early-time or late-time numerical data.

I. INTRODUCTION

Lattice QCD (LQCD) calculations of nucleon matrix elements have reached a level of maturity for inclusion in the most recent Flavour Lattice Averaging Group (FLAG) review [1]. It is now common that results are obtained with multiple lattice spacings, multiple volumes and pion masses at or near the physical pion mass. Control over the continuum, infinite volume and physical pion mass extrapolations are necessary to compare

LQCD results amongst themselves as well as with experiments.

However, there is an additional source of systematic uncertainty in the calculations which must be brought under control before the extrapolations can be relied upon, and that is the excited state contamination of the correlation functions. The source of the issue is tied to the well-known signal-to-noise (S/N) problem [2]. At early time, where the stochastic noise is under control, the correlation functions have significant contamination from excited states, while at large time, where there is ground state saturation, the noise overwhelms the signal. To date, there are no calculations of nucleon three-point functions performed at light pion masses with sufficient

* Not all in California; <https://callat-qcd.github.io>

statistics that the ground state matrix element can be determined without addressing the contributions from excited states.

The FLAG review summarizes challenges in controlling the excited state contamination in these calculations and the strategies various groups use to do so. In this article, we will focus on two important points that are not discussed in the FLAG review and which are generally lacking in the literature:

1. Stability of the ground state matrix element under the truncation of data and/or the variation in the number of excited states used in the analysis;
2. Quantification of the excited state contamination.

The first issue is generally not discussed because most calculations utilize too few values of fixed source-sink separation times (t_{sep}) for data truncation to be feasible. The limited number of t_{sep} values used also limits the number of excited states that can be removed through extrapolation due to the larger number of matrix elements needed to perform multi-state fits. In the flavor physics LQCD community, stability of the extracted ground state observable over an appreciable time range (sufficiently large to rule out correlated fluctuations) has long been recognized as crucial for ruling out excited state contamination in two-point and three-point calculations [3–7]; any residual contamination to the ground state observable from excited states will either be observed as a trend in time of its value, or is smaller than the precision with which the observable has been extracted. For nucleon correlation functions, it is even more crucial that this stability be demonstrated as they are more susceptible to correlated late-time fluctuations through their degrading S/N ratios. Care must be taken, however, to demonstrate this stability before the exponential growth of the noise erases the ability to detect time dependence in the observable.

The second issue is typically addressed qualitatively as most calculations rely upon numerical results with larger values of the source-sink separation time, where the size of the excited-state contributions are relatively smaller and the stochastic noise is larger, thus limiting the ability to obtain a controlled, quantitative understanding of the excited state contributions to the correlation function.

In order to address these issues, we have generated results with a large number of short to intermediate values of the source-sink separation time (13 values for $t_{\text{sep}} \approx 0.18 - 1.22$ fm) on an a09m310 ($a \approx 0.09$ fm, $M_\pi \approx 310$ MeV) ensemble. The large number of t_{sep} values with precise numerical results allows us to include up to five states in the correlation function analysis while performing a variety of data cuts, as discussed in detail in Sec. III.

We focus our analysis and discussion on g_A , the nucleon matrix element of the axial current in the forward limit, as this matrix element has proved to be one of the most challenging regarding control of excited state

contamination. The first LQCD calculation of g_A with relatively light dynamical quarks ($m_\pi \gtrsim 350$ MeV) appeared in 2005 [8], resulting in a value that had a 7% statistical uncertainty and agreed with the experimental value after extrapolation to the physical pion mass. This led the community to anticipate g_A would soon become a precision benchmark quantity for LQCD.

However, subsequent calculations confounded these expectations with the results remaining roughly independent of the pion mass (and below the physical value) or, worse, trending away from the physical value as the pion mass was reduced [9–11]. It was speculated that the issue might be due to finite volume corrections which were much larger than predicted by chiral perturbation theory (χ PT) [12–14]. As groups investigated the sensitivity of the extracted matrix elements as a function of t_{sep} , and added an excited state in the fit model for the correlation function, it became clear that the dominant unresolved issue was contamination from excited states [15–20]. After this, a number of calculations were performed [17, 21–34] that were in agreement with the physical value of g_A [35–44]. Following our computation with the Feynman-Hellmann method described in Ref. [45], other groups have also utilized a larger number of t_{sep} values at the physical pion mass [32, 33] and found an improved understanding of excited states.¹

Despite this progress, there remains some tension in the literature, in particular between our results [27–30] and those from the PNDME Collaboration [24, 31], both of which are the only results to utilize three (CaLat) or four (PNDME) lattice spacings and physical pion masses. Both sets of results were generated with mixed actions that use the $N_F = 2 + 1 + 1$ Highly Improved Staggered Quarks (HISQ) [48] in the sea-quark sector generated by the MILC collaboration [49] and, in the former case, also by the CaLat Collaboration [50, 51]. The CaLat results are generated with a Möbius [52] Domain-Wall [53–55] Fermion (MDWF) valence action [56] and are computed with $a \approx \{0.09, 0.12, 0.15\}$ fm lattice spacings while the PNDME results are generated with a tadpole improved [57] clover-Wilson valence action with $a \approx \{0.06, 0.09, 0.12, 0.15\}$ fm.

In Ref. [31], it was shown that the tension between the CaLat and PNDME results is driven by the PNDME results on the $a \approx 0.06$ fm ensembles, which tend to pull the final result to a smaller value, suggestive that the discrepancy may be a discretization effect. However, it was pointed out that the lever-arm in values of t_{sep} between the smallest and largest source-sink separation times was the smallest on the $a \approx 0.06$ fm ensembles, and that the high-correlation between neighboring time-slices on these fine ensembles makes them more susceptible to

¹ To the best of our knowledge, the use a large number of t_{sep} values was first advocated for in Refs. [46, 47], which demonstrated the benefit with LQCD calculations of heavy-hadron axial matrix elements using five t_{sep} values.

correlated fluctuations [58]. Further, subsequent analysis by PNDME demonstrated an under-reported excited-state fitting systematic in their results which seems to alleviate the tension [59].

Another difference between the CalLat and PNDME results is that the PNDME results rely on the more common fixed source-sink separation method while the CalLat results utilize a variant of the summation method [60] which can be derived with the Feynman-Hellmann Theorem [45]. As was shown in Ref. [17], the summation method suppresses excited states more than the standard fixed source-sink separation method, and as we will discuss in some detail in Sec. II, the Feynman-Hellmann derived correlator suppresses excited states even more than the summation method. The excited state systematic uncertainty, therefore, deserves more scrutiny, which was recognized by the community as it was the focus of the most recent review on nucleon structure from the annual lattice field theory symposium [61].

The challenge of controlling calculations of g_A and other matrix elements has inspired a series of papers aimed at understanding the excited state contamination by utilizing chiral perturbation theory [62–67]. This work has led to further ideas to try to improve the calculation of the nucleon axial form-factor [68, 69]. It is worth noting, however, that χ PT predicts that the excited state contributions should shift the correlation function above its asymptotic value, while numerical results from all calculations show that the ground state limit is approached from below, and thus, there is a significant discrepancy between this theoretical prediction and the numerical data. While there are some significant indications that $SU(2)$ baryon chiral perturbation theory, without explicit delta degrees of freedom, is not a converging expansion even at the physical pion mass [28, 30, 70–74], one might anticipate that the predictions from chiral perturbation theory should be at least qualitatively correct.

In this work, we take a data-driven approach and ask, given a large dataset, what can we learn about the excited state contamination of the nucleon axial-vector three-point function? We begin with a summary of the spectral representation of the three point functions in Sec. II, then we turn to our numerical results and analysis in Sec. III. We offer some observations and conclusions in Sec. IV, and we present extensive details of our results and analysis in the appendices.

II. SPECTRAL DECOMPOSITION

Lattice QCD calculations are performed in Euclidean space in a mixed time-momentum basis. In this paper, we focus on the forward matrix element at zero momentum. Most LQCD calculations are performed with a local creation operator and a momentum-space annihilation operator. With such a setup, the relevant two-point correlation function at zero momentum and time separation

t_{sep} is given by

$$\begin{aligned} C_2(t_{\text{sep}}) &= \sum_{\mathbf{x}} \langle \Omega | N(t_{\text{sep}}, \mathbf{x}) N^\dagger(0, \mathbf{0}) | \Omega \rangle \\ &= \sum_{n=0}^{\infty} |z_n|^2 e^{-E_n t_{\text{sep}}} \\ &= |z_0|^2 e^{-E_0 t_{\text{sep}}} \left[1 + \sum_{n=1}^{\infty} |r_n|^2 e^{-\Delta_{n0} t_{\text{sep}}} \right]. \end{aligned} \quad (1)$$

In this expression, we assume that the overlap factors, $z_n = \langle \Omega | N | n \rangle$, used to create (N^\dagger) and annihilate (N) the states with quantum numbers of the nucleon from the vacuum ($|\Omega\rangle$) are conjugate to each other.² In the last line, we have defined the energy splitting and ratio of overlap factors:

$$\Delta_{mn} = E_m - E_n, \quad r_n = \frac{z_n}{z_0}. \quad (2)$$

The parameterization of Eq. (1) recasts all excited-state parameters with respect to the ground-state, and yields a more universal set of excited-state distributions, simplifying the estimation of their starting values in a frequentist minimization or prior distribution in a Bayesian minimization [75].

A. Three-point correlators

The matrix elements of interest (with Dirac structure Γ) are determined through an analysis of three-point correlation functions which are also computed in a mixed time-momentum basis. The most common strategy is to use a sink with fixed definite spatial momentum at $t = t_{\text{sep}}$ with a current insertion (j_Γ) at τ inbetween the source (N^\dagger) at $t = 0$ and the sink (N). In the limit of zero momentum and zero-momentum transfer, the three-point function is given by

$$\begin{aligned} C_\Gamma(t_{\text{sep}}, \tau) &= \sum_{\mathbf{y}, \mathbf{x}} \langle \Omega | N(t_{\text{sep}}, \mathbf{y}) j_\Gamma(\tau, \mathbf{x}) N^\dagger(0, \mathbf{0}) | \Omega \rangle \\ &= \sum_n |z_n|^2 g_{nn}^\Gamma e^{-E_n t_{\text{sep}}} \\ &\quad + 2 \sum_{n < m} z_n z_m^\dagger g_{nm}^\Gamma e^{-(E_n + \frac{\Delta_{mn}}{2}) t_{\text{sep}}} \\ &\quad \times \cosh \left[\Delta_{mn} \left(\tau - \frac{t_{\text{sep}}}{2} \right) \right], \end{aligned} \quad (3)$$

where the matrix elements of interest are given by

$$g_{mn}^\Gamma = \langle m | j_\Gamma | n \rangle, \quad (4)$$

² We are using the non-relativistic normalization $\langle n | m \rangle = \delta_{nm}$ and $\mathbf{1} \equiv |\Omega\rangle \langle \Omega| + \sum_{n=0}^{\infty} |n\rangle \langle n|$. We assume that the contributions from the thermal bath or alternate temporal boundary conditions are sufficiently suppressed that they can be ignored.

and we have assumed

$$z_n z_m^\dagger g_{nm}^\Gamma = z_m z_n^\dagger g_{mn}^\Gamma, \quad (5)$$

which holds in the forward limit at zero momentum.

ANDRÉ: I assume this is true - haven't checked

Typically one determines the ground state matrix element, g_{00}^Γ , by performing the computation for 1, 2, 3 or sometimes 4 values of t_{sep} in the range $t_{\text{sep}} \approx 1 - 1.5$ fm while utilizing local three-quark interpolating fields for the creation and annihilation operators. The correlation functions are then analyzed using models with zero, one, or more excited states [17, 21–34], with some analysis using up to four states [59, 76, 77]. There are several challenges and shortcomings with this strategy, which we will summarize. However, one should note that this method has been used, as so far, it has seemed the most economical. Improvements upon this strategy would require a substantial increase in computational complexity, effort to employ, and amount of computing resources.

The ground state (gs) matrix element g_{00}^Γ is typically determined by constructing the ratio correlation function

$$R_\Gamma(t_{\text{sep}}, \tau) = \frac{C_\Gamma(t_{\text{sep}}, \tau)}{C_2(t_{\text{sep}})}, \quad (6)$$

which gives the ground state in the limit

$$\lim_{t_{\text{sep}} \rightarrow \infty} R_\Gamma(t_{\text{sep}}, \tau \approx t_{\text{sep}}/2) = g_{00}^\Gamma. \quad (7)$$

The energies and overlap factors can be constrained from the two-point function, leaving the three-point function to constrain the matrix elements g_{nn}^Γ and g_{nm}^Γ .³ From Eq. (3), one observes that only the transition terms ($n \neq m$) are sensitive to the current insertion time τ . To isolate the ground state matrix element, the minimum number of values of t_{sep} required is at least one greater than the number of states used in the analysis in order to have a 1-degree-of-freedom fit. For example, a two-state fit requires the determination of g_{00}^Γ , g_{11}^Γ and g_{01}^Γ : the latter can be constrained from the τ dependence leaving the remaining t_{sep} dependence to constrain the former two matrix elements. In this minimum scenario, computations which utilize three values of t_{sep} (or less) are not able to perform a systematic study on omitting values of t_{sep} , or changing the number of states used in the analysis. This prohibits a verification that the full uncertainty on g_{00}^Γ associated with this excited state contamination has been correctly captured. In other words, we would have to assign an unquantified systematic uncertainty to the ground state matrix element.

Another significant challenge is that lattice computations of three-point functions are typically performed for

$t_{\text{sep}} \gtrsim 1$ fm, which is roughly the time separation when the stochastic noise is becoming significant. Again, because of the limited values of t_{sep} typically used, one cannot determine if the data at this time is susceptible to a correlated fluctuation or not, which, if present, would cause a bias in the results. We will return to this point in Sec. III.

To understand the various sources of excited state (es) contamination, we reorder Eq. (6) in a way which deliberately disentangles the different types of excited state contributions. For the two-point correlation function, it is straightforward to separate the ground state from the excited states

$$\begin{aligned} C_2(t_{\text{sep}}) &= C_2^{\text{gs}}(t_{\text{sep}}) + C_2^{\text{es}}(t_{\text{sep}}), \\ C_2^{\text{gs}}(t_{\text{sep}}) &= |z_0|^2 e^{-E_0 t_{\text{sep}}}, \\ C_2^{\text{es}}(t_{\text{sep}}) &= \sum_{n \geq 1} |z_n|^2 e^{-E_n t_{\text{sep}}}. \end{aligned} \quad (8)$$

For the three-point functions, we define the n -to- n as scattering (sc) states and the n -to- m as transition (tr) states such that

$$\begin{aligned} C_\Gamma(t_{\text{sep}}, \tau) &= C_\Gamma^{\text{gs}}(t_{\text{sep}}) + C_\Gamma^{\text{sc}}(t_{\text{sep}}) + C_\Gamma^{\text{tr}}(t_{\text{sep}}, \tau), \\ C_\Gamma^{\text{gs}}(t_{\text{sep}}) &= |z_0|^2 g_{00}^\Gamma e^{-E_0 t_{\text{sep}}}, \\ C_\Gamma^{\text{sc}}(t_{\text{sep}}) &= \sum_{n \geq 1} |z_n|^2 g_{nn}^\Gamma e^{-E_n t_{\text{sep}}}, \\ C_\Gamma^{\text{tr}}(t_{\text{sep}}, \tau) &= \sum_{n < m} z_n z_m^\dagger 2g_{nm}^\Gamma e^{-(E_n + \frac{\Delta_{mn}}{2})t_{\text{sep}}} \\ &\quad \times \cosh \left[\Delta_{mn} \left(\tau - \frac{t_{\text{sep}}}{2} \right) \right]. \end{aligned} \quad (9)$$

The ratio correlation function can then be expressed as

$$\begin{aligned} R_\Gamma(t_{\text{sep}}, \tau) &= g_{00}^\Gamma + \frac{C_\Gamma^{\text{sc}}(t_{\text{sep}}) - g_{00}^\Gamma C_2^{\text{es}}(t_{\text{sep}})}{C_2(t_{\text{sep}})} \\ &\quad + \frac{C_\Gamma^{\text{tr}}(t_{\text{sep}}, \tau)}{C_2(t_{\text{sep}})} \\ &= g_{00}^\Gamma + \frac{\sum_{n \geq 1} (g_{nn}^\Gamma - g_{00}^\Gamma) |z_n|^2 e^{-E_n t_{\text{sep}}}}{C_2(t_{\text{sep}})} \\ &\quad + \frac{C_\Gamma^{\text{tr}}(t_{\text{sep}}, \tau)}{C_2(t_{\text{sep}})}. \end{aligned} \quad (10)$$

Consider the leading excited state contamination to g_{00}^Γ arising from g_{11}^Γ , and g_{01}^Γ

$$\begin{aligned} R_\Gamma(t_{\text{sep}}, \tau) &\approx g_{00}^\Gamma + |r_1|^2 (g_{11}^\Gamma - g_{00}^\Gamma) e^{-\Delta_{10} t_{\text{sep}}} \\ &\quad + 2r_1^\dagger g_{01}^\Gamma e^{-\Delta_{10} \frac{t_{\text{sep}}}{2}} \cosh \left[\Delta_{10} \left(\tau - \frac{t_{\text{sep}}}{2} \right) \right] \\ &\quad + \dots \end{aligned} \quad (11)$$

where the \dots includes terms from higher excited states as well as from the first excited state, but further suppressed by extra powers of $\exp(-\Delta_{10} t_{\text{sep}})$. The scattering and two-point excited state contributions, in addition to

³ Some groups fix the overlap factors and energies from the two-point correlation function and then pass the central or correlated values into a three-point function analysis. Instead, we perform a simultaneous fit to the two- and three-point functions.

cancelling against each other for same-sign values of g_{11}^Γ and g_{00}^Γ , are suppressed by the full t_{sep} , $\exp(-\Delta_{10}t_{\text{sep}})$. In contrast, the transition excited states are only suppressed by half the time separation, $\exp(-\Delta_{10}\frac{t_{\text{sep}}}{2})$, and so they are expected to be the dominant source of excited state contamination.

B. Feynman-Hellmann and Summed Correlators

Rather than analyzing the three-point functions, one can construct a correlation function in which the current insertion time is summed over

$$\begin{aligned} \Sigma_\Gamma(t_{\text{sep}}, \tau_c) &= \sum_{\tau=\tau_c}^{t_{\text{sep}}-\tau_c} C_\Gamma(t_{\text{sep}}, \tau) \\ &= \sum_n |z_n|^2 (t_{\text{sep}} + 1 - 2\tau_c) g_{nn}^\Gamma e^{-E_n t_{\text{sep}}} \\ &\quad + 2 \sum_{n < m} z_n z_m^\dagger g_{nm}^\Gamma e^{-(E_n + \frac{\Delta_{mn}}{2})t_{\text{sep}}} \\ &\quad \times \frac{\sinh\left[\frac{\Delta_{mn}}{2}(t_{\text{sep}} + 1 - 2\tau_c)\right]}{\sinh\left(\frac{\Delta_{mn}}{2}\right)}. \end{aligned} \quad (12)$$

The original implementation of the idea included a sum over all timeslices, including when the the time ordering of the current was before the source and after the sink as well as equal to the source ($\tau = 0$) and sink ($\tau = t_{\text{sep}}$) where contact terms arise [60]. Given a set of fixed source-sink separation datasets, one is of course free to perform the sum in a variety of ways, e.g. excluding data from the out-of-time-order regions, excluding the source and sink time (setting $\tau_c = 1$ in Eq. (12)) or also cutting time near the source and sink ($\tau_c > 1$).

The summed correlation function at large t_{sep}

$$\begin{aligned} \Sigma_\Gamma(t_{\text{sep}}, \tau_c) &= |z_0|^2 e^{-E_0 t_{\text{sep}}} \left\{ \right. \\ &\quad (t_{\text{sep}} + 1 - 2\tau_c) \left[g_{00}^\Gamma + |r_1|^2 g_{11}^\Gamma e^{-\Delta_{10} t_{\text{sep}}} \right] \\ &\quad \left. + r_1^\dagger g_{01}^\Gamma \frac{e^{\frac{\Delta_{10}}{2}(1-2\tau_c)} - e^{-\Delta_{10}(t_{\text{sep}} + \frac{1}{2} - \tau_c)}}{\sinh(\frac{\Delta_{10}}{2})} \right\} + \dots, \end{aligned} \quad (13)$$

can be used to determine the leading excited state contamination. Of note, the ground state and the scattering (n -to- n) states are relatively enhanced by $t_{\text{sep}} + 1 - 2\tau_c$. The transition matrix elements (m -to- n) lead to a t_{sep} independent term and those that depend upon t_{sep} become exponentially suppressed by the full excited state gap ($e^{-\Delta_{10}t_{\text{sep}}}$) rather than half the gap, as with the three-point function, Eq. (11), as noted in Ref. [17]. Thus, one expects that the excited state contamination of the summed correlation function is smaller than for the standard fixed source-sink separation time three-point correlation function, up to this t_{sep} independent term.

This summed correlation function has received some attention in the literature [17, 78–80]. More recently,

there have been calculations which utilize a Feynman-Hellmann approach, by performing a computation in the presence of background fields and extracting the matrix elements through the linear response of the spectrum to the background field [81–83]. In Ref. [45], it was shown that the application of the Feynman-Hellmann theorem to the effective mass directly leads to a derivative of the summed correlation function [60], relating the matrix element to the spectrum without the need for an explicit background field. We call this the Feynman-Hellmann (FH) correlation function⁴

$$\begin{aligned} \text{FH}_\Gamma(t_{\text{sep}}, \tau_c, dt) &= \sum_{\tau=\tau_c}^{t_{\text{sep}}-\tau_c} \frac{R_\Gamma(t_{\text{sep}} + dt, \tau) - R_\Gamma(t_{\text{sep}}, \tau)}{dt} \\ &= \frac{1}{dt} \left[\frac{\Sigma_\Gamma(t_{\text{sep}} + dt, \tau_c)}{C_2(t_{\text{sep}} + dt)} - \frac{\Sigma_\Gamma(t_{\text{sep}}, \tau_c)}{C_2(t_{\text{sep}})} \right], \\ \text{FH}_\Gamma(t_{\text{sep}}, \tau_c) &\equiv \text{FH}_\Gamma(t_{\text{sep}}, \tau_c, dt = 1). \end{aligned} \quad (14)$$

Since the FH correlation function is constructed from $\Sigma_\Gamma(t_{\text{sep}}, \tau_c)$, it enjoys the larger suppression of excited states, with the leading excited state contamination scaling as $\exp(-\Delta_{10}t_{\text{sep}})$ rather than with $\Delta_{10}/2$ (the t_{sep} independent pieces exactly cancel in the numerical derivative). Additionally, this numerical derivative serves to both isolate the ground state, whose contribution grows linearly in t_{sep} , as well as to further suppress the scattering (n -to- n) and transition (m -to- n) excited states which do not strongly differ from one timeslice to the next. This stronger suppression of excited states is what allowed us to utilize earlier Euclidean time data [27–29] than is common in the three-point correlation function analysis and to enjoy the benefits of the lower stochastic noise. We will show this in some details in Sec. III A.

III. LATTICE CALCULATION

For the present study, we use results from our MDWF on gradient-flowed HISQ action [56] on the a09m310 ensemble, which has a lattice spacing of $a \approx 0.09$ fm and a pion mass of $m_\pi \approx 310$ MeV. We use the same parameters as in Refs. [27, 28, 56] except for the quark-smearing, we use the parameters $\sigma_{\text{smr}} = 3.5$ and $N_{\text{smr}} = 45$ that go in the GAUGE_COVARIANT_GAUSSIAN smearing routine in Chroma [84].

We generate 16 sources per gauge configuration on 784 configurations. We generate the three-point functions using a sequential-propagator through the sink at 13 values of t_{sep} ,

$$t_{\text{sep}}/a_{09} \in \{2, 3, 4, 5, 6, 7, 8, 9, 10, 11, 12, 13, 14\}. \quad (15)$$

⁴ In the original implementation [45], the sum over the current time is over all time-slices, which we denote $\tau_c = \text{none}$, as in the original summation method [60].

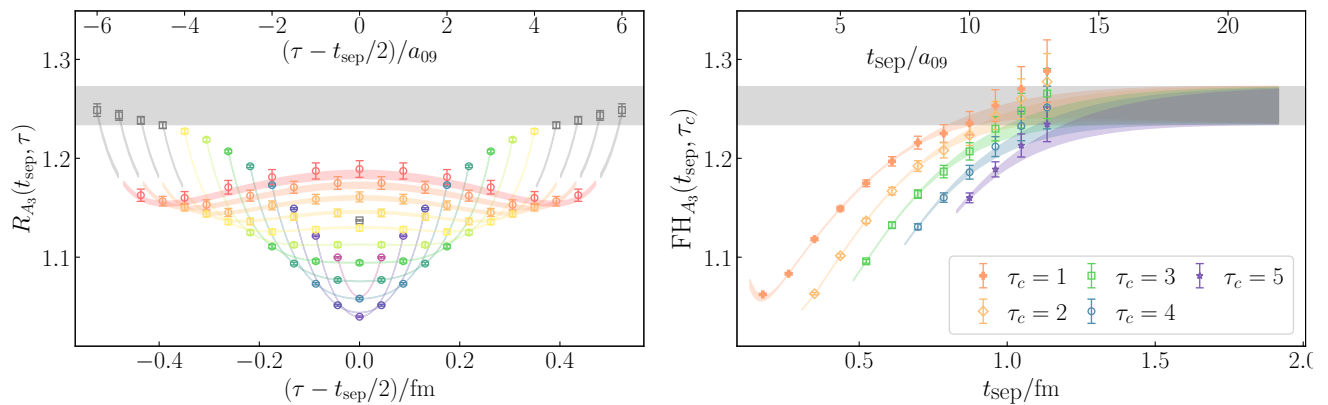


FIG. 1. Left: (Psychedelic Moose/Water Buffalo plot) We plot the numerical results of $R_{A_3}(t_{\text{sep}}, \tau)$ for $t_{\text{sep}} = 2$ (the single gray point in the middle) to $t_{\text{sep}} = 14$, the top (red) dataset. In addition, we plot the resulting posterior description of the correlation function from our 5-state fit as the (correspondingly colored) fit bands. The (gray) squares in the upper left/right of the “moose antlers” are not included in the analysis, as indicated by the break in the fit band from the inner region. The horizontal (gray) band is the ground state matrix element, \hat{g}_A . Right: The $\text{FH}_{A_3}(t_{\text{sep}}, \tau_c = 1)$ numerical data from the global analysis is plotted along with the posterior description of the correlation function. The time-axis is converted from lattice units (top) to fm (bottom) using our scale-setting [51].

Our sources and sinks are generated with a local three-quark interpolating field using only the upper-spin components of the quark field in the Dirac-Pauli basis (lower components for the negative parity states), which was shown to give the largest overlap onto the ground state of the nucleon at rest [85, 86]. In App. A, we present further details of our computation such as the cost benefit analysis of improving the stochastic sampling by combining 8 coherent sinks [10] for each sequential propagator, the use of spin up and spin down sources and sinks (versus utilizing a spin-projector that isolates one of the spin states) and the use of time-reversed negative parity correlators.

A. Full results

We begin with a presentation of our final results which come from a fully-correlated Bayesian constrained curve-fitting [3] with a five-state model to describe

$$C_2(t_{\text{sep}}), \quad R_{A_3}(t_{\text{sep}}, \tau), \quad R_{V_4}(t_{\text{sep}}, \tau), \\ \text{FH}_{A_3}(t_{\text{sep}}, \tau_c = 1), \quad \text{FH}_{V_4}(t_{\text{sep}}, \tau_c = 1).$$

The final result is obtained with all values of τ between the source and sink time, $\tau = [1, t_{\text{sep}} - 1]$. For $R_\Gamma(t_{\text{sep}}, \tau)$, the results are symmetrized about $\tau = t_{\text{sep}}/2$ and half the data (plus $\tau = t_{\text{sep}}/2$ point for even values of t_{sep}) is used in the analysis.

In the left panel of Fig. 1 (the “Psychedelic Moose”), we plot the numerical results for the ratio of the three-point function generated with the $A_3 = \bar{q}\gamma_3\gamma_5\tau_3q$ current, divided by the two-point function at the given value of t_{sep} (cfr. Eq. (6)). We also plot the resulting posterior description with our 5-state model. The fit quality is good and visually one can see that the model accurately

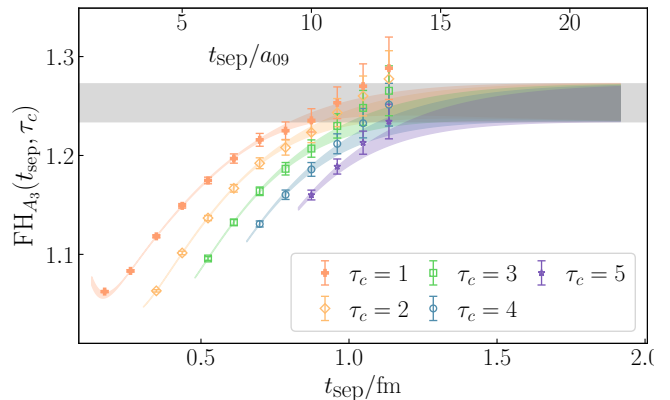


FIG. 2. We plot the numerical $\text{FH}_{A_3}(t_{\text{sep}}, \tau_c)$ data for various values of τ_c as well as the posterior reconstruction of these correlation functions from the global analysis that uses $\tau_c = 1$.

describes the numerical results over the full range of t_{sep} and τ used in the analysis. The horizontal (gray) band is the value of the ground state matrix element \hat{g}_A . In the right panel we plot the $\text{FH}_{A_3}(t_{\text{sep}}, \tau_c = 1)$ data that are used in the global fit as well as the resulting posterior distribution of this correlation function.

In Fig. 2, we explore the $\text{FH}_{A_3}(t_{\text{sep}}, \tau_c)$ data as the number of data near the source and sink time are cut from the sum over current insertion time denoted by increasing τ_c . The posterior fit bands are from the global analysis that uses $\tau_c = 1$. As τ_c is increased, for a fixed t_{sep} , one observes that the excited state contribution becomes larger. This can be understood by looking at the leading excited state contribution to $\text{FH}_\Gamma(t_{\text{sep}}, \tau_c)$ that depends

upon τ_c

$$\text{FH}_\Gamma(t_{\text{sep}}, \tau_c) \ni e^{\Delta_{10}(\tau_c + \frac{1}{2})} r_1^\dagger g_{01}^\Gamma \frac{e^{-\Delta_{10}t_{\text{sep}}} - e^{-\Delta_{10}(t_{\text{sep}}+1)}}{\sinh \frac{\Delta_{10}}{2}}.$$

As is evident from Fig. 1, which is common to all LQCD calculations of g_A , the transition matrix element $g_{01}^{A_3} < 0$. Therefore, the leading excited state contamination that depends upon τ_c is negative and grows exponentially with increasing τ_c , consistent with the results.

In order to have confidence in our final results for $m_N = E_0$, \hat{g}_A and \hat{g}_V ,⁵ as well as the ability to quantify and control the excited state contamination, we discuss our analysis strategy and the stability of our results under model-variation and data truncation.

B. Analysis strategy

We have two goals with this work:

1. Identify the ground state mass and matrix elements, \hat{g}_A (and \hat{g}_V), with a complete systematic uncertainty;
2. Obtain a quantitative understanding of the excited state contamination of the correlation functions used in the analysis.

The former is possible without the latter through a demonstration that the extracted ground state mass and matrix elements are invariant under modifications of the fit model (i.e. the number of excited states and the model of their mass-gap) and truncations in the time range used in the analysis.

A robust identification of the excited state spectrum and matrix elements would require the use of a variational basis that includes multi-hadron operators [87–89]. For this reason, our second goal is to obtain a quantitative understanding of the sum of all excited state contributions, and in particular, to quantify how they contaminate the ground state values. To achieve this goal it is essential that the fit model accurately describes the correlation function over the full range of time separations without over-fitting the data.

In App. B, we provide a detailed description of the analysis and the sensitivity of the ground state posteriors under variations in the number of states used, the model of excited states and the fit ranges in t_{sep} and τ . Here, we summarize the findings of this study.

We begin with a discussion of the model for the excited states. The lowest-lying excited states consist roughly of either a nucleon-pion in a relative P-wave or a nucleon with a two-pion excitation. With $m_\pi L \approx 4$ the non-interacting energy levels of these two states are nearly

identical and so a calculation without multi-hadron operators can not distinguish them. Therefore, they are treated as a single excited state. We then use three different models for the spectrum of excitations and parametrize the energy gaps ΔE_n , where n indicates the n^{th} state, as:

$$\begin{aligned} n^{\text{th}} \text{ energy level} & E_n = E_0 + \sum_{l=1}^n \Delta E_l, \\ \text{harmonic oscillator (HO)} & \Delta E_n = 2m_\pi, \\ \text{inverse } n \text{ (1/n)} & \Delta E_n = 2m_\pi/n, \\ \text{inverse } n^2 \text{ (1/n}^2\text{)} & \Delta E_n = 2m_\pi/n^2. \end{aligned} \quad (16)$$

For each model, for each level $n < N_{\text{max}}$, we set the prior as $\Delta \tilde{E}_n = (\Delta E_n, m_\pi)$ where the first entry is the prior mean and the second is the prior width. For the highest state, which we expect to be a “garbage can”, we set the prior width to be $5m_\pi$. We observe two important facts when we vary the excited state model:

1. The ground state posteriors are insensitive to the model used;
2. The excited state posteriors are mostly insensitive to the model used, even when the posterior is in significant conflict with the prior. This is a strong indicator that the extracted energy levels are dictated by the numerical data and not the priors used.

In Fig. 3, we show the sensitivity of \hat{g}_A and the spectrum on the excited state model versus the $t_{\text{sep}}^{\text{min}}$ of the two-point correlation function (in all cases for the full five-state, five-correlation function analysis). The lowest panel is the relative weight determined from the three models at a given $t_{\text{sep}}^{\text{min}}$

$$w_i = \frac{e^{\log \text{GBF}_i}}{\sum_{j \in \text{models}} e^{\log \text{GBF}_j}}, \quad (17)$$

where $\log \text{GBF}$ is the log of the Gaussian Bayes Factor. The next panel gives the $Q \in [0, 1]$ value which is a measure of the fit-quality. For the values of \hat{g}_A and E_n , the light (red) horizontal band is the value of the given quantity from the chosen fit from the HO model at $t_{\text{sep}}^{\text{min}} = 3$, to guide the eye, which is also denoted by the markers with a black border. The vertical bars represent the prior width for the given quantity and are aligned in the same vertical column as their corresponding posterior values (for \hat{g}_A and E_0 , the prior widths are larger than the displayed y -limits and so they are not shown).⁶ Finally, the horizontal dashed lines give the non-interacting P -wave

⁵ With our action, the axial-vector and vector renormalization factors are equal to 10^{-4} so the renormalized axial charge is given by the ratio of the bare matrix elements, $g_A = \hat{g}_A/\hat{g}_V$ [28].

⁶ The energy spectrum is priored with a series of ordered energy splittings. Therefore, to construct the priors shown in Fig. 3, we plot $\tilde{E}_n = \tilde{E}_0 + \sum_{l=1}^{n-1} \Delta \tilde{E}_l + \Delta \tilde{E}_n$ where the priors are denoted with a tilde and the posteriors are denoted with a hat.

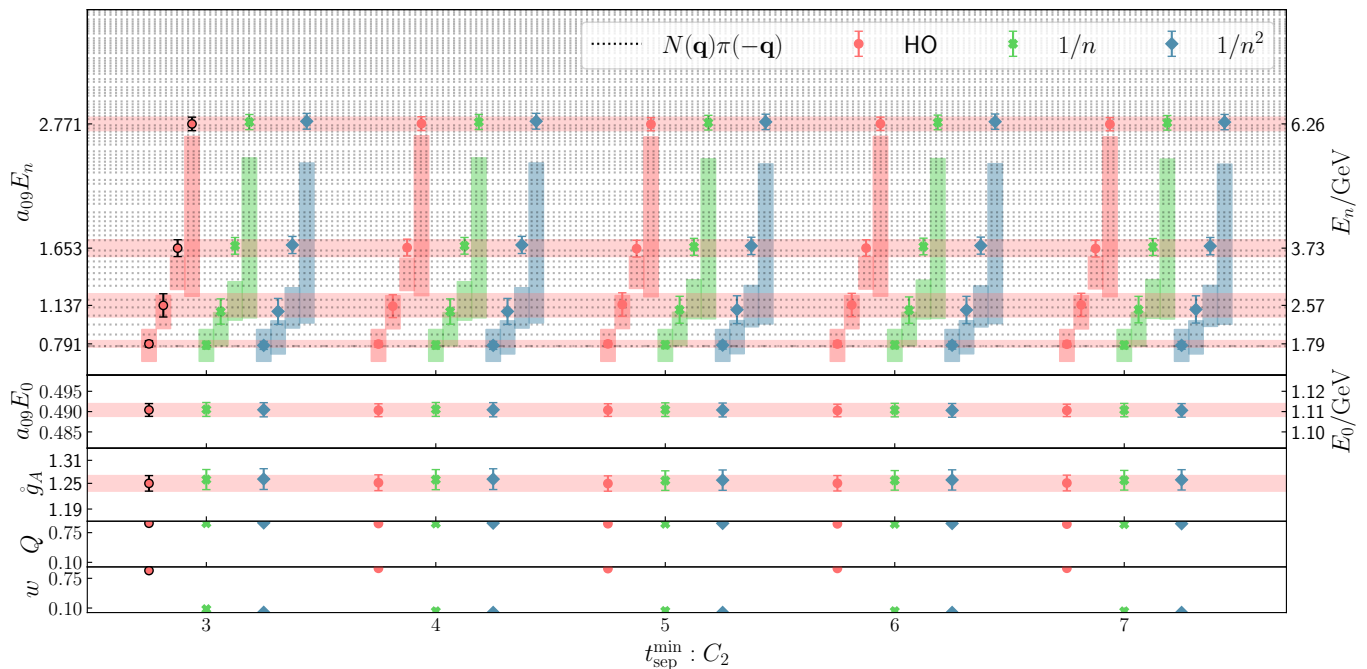


FIG. 3. Sensitivity of the extracted spectrum and \hat{g}_A on the model of excited states used as a function of $t_{\text{sep}}^{\text{min}}$ in the $C_2(t_{\text{sep}})$ correlation function. For a given $t_{\text{sep}}^{\text{min}}$, from left to right, offset for visual clarity, we plot the prior (vertical (colored) box) and posterior values (filled markers) of \hat{g}_A , E_0 and E_n for the harmonic-oscillator (HO), inverse n ($1/n$) and inverse n^2 ($1/n^2$) excited state models, Eq. (16). The prior width on \hat{g}_A and E_0 are larger than the displayed y -limits, and thus not shown. The horizontal light (red) bands (to guide the eye) are from the chosen fit denoted with the black-border on the markers. The horizontal dashed lines denote the non-interacting energy levels of the P -wave $N\pi$ states. See the text for more details.

$N(\mathbf{q})\pi(-\mathbf{q})$ energy levels, which one can see are quite dense. The lowest non-interacting $N(\mathbf{q} + \mathbf{p})\pi(-\mathbf{q})\pi(-\mathbf{p})$ level where all hadrons are at rest is nearly degenerate with the lowest $N(\mathbf{q})\pi(-\mathbf{q})$ level. Of note,

1. The extracted posteriors are consistent between models which all have a high fit-quality, even when the posterior value is in tension with the prior. This is a strong indicator the extracted spectrum is highly constrained by the numerical data and not the priors, even for the high-lying energy levels.
2. The first excited state is consistent with the lowest lying $N\pi$ state (which is nearly degenerate with the $N\pi\pi$ state). The higher lying states have an uncertainty that spans several anticipated energy levels, indicating that they are likely a linear combination of eigenstates.

Next, we examine the stability of \hat{g}_A as we remove data from the fit (all fits still use the set of five correlation functions). We examine the sensitivity as we increase $t_{\text{sep}}^{\text{min}}$ in the analysis, as we reduce $t_{\text{sep}}^{\text{max}}$ and also through using only even or odd values of t_{sep} in the three-point functions. For each choice of which values of t_{sep} to use, $\text{FH}_\Gamma(t_{\text{sep}}, \tau_c = 1, dt)$ is constructed from the set of $R_\Gamma(t_{\text{sep}}, \tau)$. When we use consecutive values of t_{sep} , we take $dt = 1$ in $\text{FH}_\Gamma(t_{\text{sep}}, \tau_c = 1, dt)$. When we use only even or odd values of t_{sep} , we take $dt = 2$.

The left panel of Fig. 4 shows \hat{g}_A as a function of the minimum and maximum value of t_{sep} used in the analysis. When $t_{\text{sep}}^{\text{min}}$ is varied, $t_{\text{sep}}^{\text{max}}$ is held fixed at 14. When $t_{\text{sep}}^{\text{max}}$ is varied, $t_{\text{sep}}^{\text{min}}$ is fixed at 2. In the middle panel of Fig. 4, we show the value of \hat{g}_A as a function of $t_{\text{sep}}^{\text{max}}$ when only even values of t_{sep} are used in the analysis of $R_\Gamma(t_{\text{sep}}, \tau)$ and $\text{FH}_\Gamma(t_{\text{sep}})$. The right panel is the same as the middle one except we only use the odd values of t_{sep} in the analysis.

When the three-point functions are computed with a sufficiently large number of t_{sep} values, the ground state parameters are very stable under data truncation and the excited state model. Of note, it is sufficient to use every other value of t_{sep} at this $a \approx 0.09$ fm lattice spacing.

C. Excited State Breakdown

Given a model that is demonstrated to accurately describe the correlation functions over the full range of t_{sep} and τ used in the analysis, we can separate the various sources of excited state contamination into the “scattering” (n -to- n) and “transition” (m -to- n) sources as well as those arising from the excited states of the two-point function (see Sec. II A). While we can accurately describe these various sources of excited state contamination, we can not claim to have a rigorous determination of the spectrum, since the creation and annihilation oper-

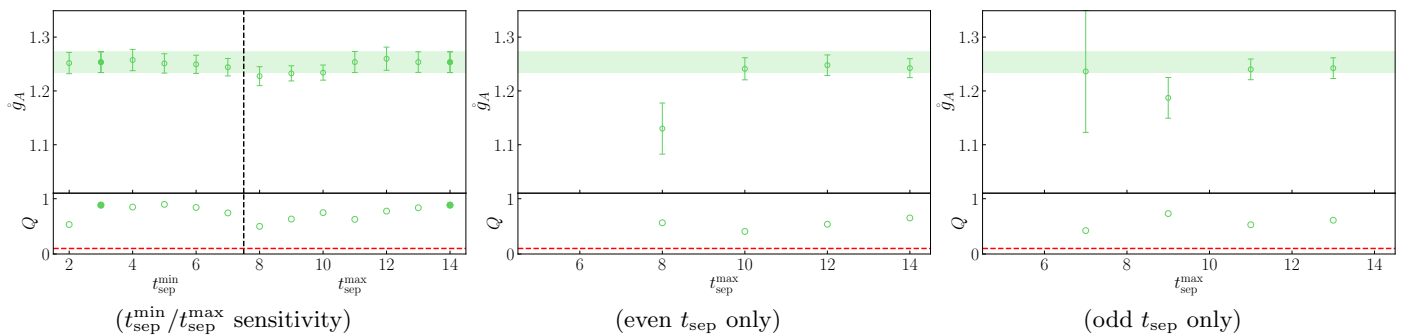


FIG. 4. Stability of the determination of \hat{g}_A under data truncation. The horizontal band is the value of \hat{g}_A determined from the full analysis, to guide the eye. The bottom part of each panel represents the fit quality $Q \in [0, 1]$. The left panel shows the stability as we increase $t_{\text{sep}}^{\text{min}}$ while holding $t_{\text{sep}}^{\text{max}} = 14$ to the left of the vertical dashed line and, similarly, the result as $t_{\text{sep}}^{\text{max}}$ is increased with $t_{\text{sep}}^{\text{min}} = 2$ to the right of the dashed line. The middle and right panels show the $t_{\text{sep}}^{\text{max}}$ stability when only even or odd values of t_{sep} are used in $R_{\Gamma}(t_{\text{sep}}, \tau)$ and $\text{FH}_{\Gamma}(t_{\text{sep}}, \tau_c = 1, dt = 2)$.

ators we have used are purely local three-quark operators which are known to have poor overlap with the nucleon scattering states [88]. However, since only the transition excited states depend upon the current insertion time τ , we can confidently separate the excited states into these various classes of excited state contamination.

In Fig. 5, we plot the percent contamination of various sources of excited state contamination of the ground state for $R_{A_3}(t_{\text{sep}}, \tau = t_{\text{sep}}/2)/\hat{g}_A$ (left) and $\text{FH}_{A_3}(t_{\text{sep}}, \tau_c = 1)/\hat{g}_A$ (right). From these plots, there are several observations and conclusions one can make:

1. There is a significant cancellation between the scattering excited states and two-point excited states;
2. The transition excited states are the dominant source of excited states and they are relative suppressed in $\text{FH}_{A_3}(t_{\text{sep}}, \tau_c)$ as compared to $R_{A_3}(t_{\text{sep}}, \tau = t_{\text{sep}}/2)$;
3. The total excited state contamination at $t_{\text{sep}} \approx 1$ fm is $\approx 8\%$ for $R_{A_3}(t_{\text{sep}}, \tau = t_{\text{sep}}/2)$ and $\approx 1\%$ for $\text{FH}_{A_3}(t_{\text{sep}}, \tau_c)$.

In Eq. (10) we see an explicit cancellation between the scattering (3pt sc) and two-point excited state (2pt es) contamination, as is implied from the proportionality of the n^{th} excited state to $g_{nn}^{\Gamma} - g_{00}^{\Gamma}$. In order for this cancellation to be significant, as observed in the posterior determination of the two classes of excited states, one explanation is that $g_{nn}^{\Gamma} \approx g_{00}^{\Gamma}$ for all n . For the vector current, we know that in infinite volume, the vector operator measures the iso-vector charge of the system, which in the isospin limit, is exactly equal to g_{00}^V . It has further been demonstrated that in the forward scattering limit, the finite volume interaction amplitudes conspire with the finite volume Lellouch-Lüscher factors to ensure that $g_{nn}^{\Gamma} = g_{00}^{\Gamma}$ for two-particle states [90].

This result, while not surprising, demonstrates charge conservation in finite volume by allowing one to relate n -point Greens functions to $(n-1)$ -point Greens functions through the Ward-Takahashi equations. In the case of the axial-vector matrix element, it is plausible that in the

forward scattering limit, the corrections to such a relation arising from the partially conserved nature of the axial-vector current would also vanish, such that in this limit, the Lellouch-Lüscher factors are similarly removed. For example, for the nucleon, we know the induced pseudo-scalar form factor vanishes in the forward limit. We leave a detailed study of this question to future work.

In the left panel of Fig. 5 we see that the scattering excited state contribution (the upper (red) band/data) are roughly equal and opposite in sign to the excited states coming from the two-point function (the middle (purple) band/data). The hatched curve which is mostly white with gray hash lines, is the sum of these two contributions and it lies between them. We observe that the sum of these two sources of excited state contributions decay to a 1% correction (the horizontal dashed (red) lines) at $t_{\text{sep}} \approx 1$ fm. In contrast, the transition (3pt tr) excited states depicted by the lowest (blue) band/data do not decay to the 1% level until $t_{\text{sep}} \approx 2.2$ fm.

In the right panel of Fig. 5 we show the same excited state breakdown for the Feynman-Hellmann correlation function. Of note, the sign of the scattering and two-point excited state contributions are opposite of what they are for $R_{A_3}(t_{\text{sep}}, \tau = t_{\text{sep}}/2)$. This sign change can be understood from Eq. (14). It is also interesting to note that the magnitude of the transition excited state contributions at $t_{\text{sep}} \approx 1$ fm go from $\approx 7.5\%$ for $R_{A_3}(t_{\text{sep}}, \tau = t_{\text{sep}}/2)$ to $\approx 2.5\%$ for $\text{FH}_{A_3}(t_{\text{sep}}, \tau_c = 1)$. Finally, for $R_{A_3}(t_{\text{sep}}, \tau = t_{\text{sep}}/2)$, the sum of the scattering and two-point excited state contributions are equal in sign to the transition excited states, while for $\text{FH}_{A_3}(t_{\text{sep}}, \tau_c = 1)$ they are opposite in sign at intermediate and large t_{sep} . Thus, the total excited state contamination decays to the 1% level for the Feynman-Hellmann correlation function at $t_{\text{sep}} \approx 1$ fm while this does not happen till $t_{\text{sep}} > 2$ fm for $R_{A_3}(t_{\text{sep}}, \tau = t_{\text{sep}}/2)$. There is no proof that this fortunate cancellation must happen, however, an examination of our results in Ref. [28] shows a consistent picture that the excited state contamination of the $\text{FH}_{A_3}(t_{\text{sep}}, \tau_c = \text{none})$ correlation function decays

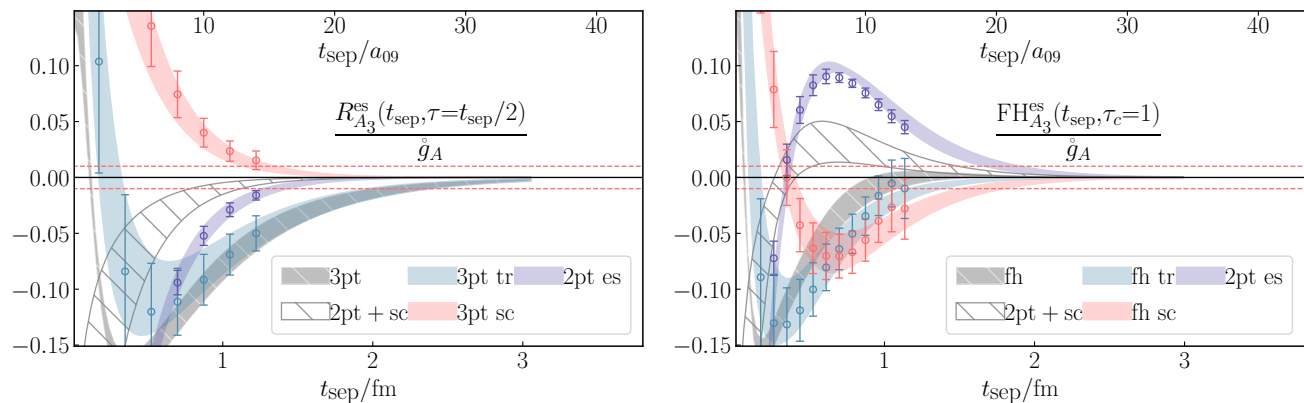


FIG. 5. Ratio of excited state contributions to the ground state contribution for $R_{A_3}(t_{\text{sep}}, \tau)$ (left, 3pt) and $\text{FH}_{A_3}(t_{\text{sep}}, \tau_c = 1)$ (right, fh). Each panel contains three types of data points: the n -to- n scattering (sc) excited states, the n -to- m transition (tr) excited states, and the excited states from the two-point (2pt es) function. The separation of the numerical data into these three classes of excited state contamination depends upon our posterior reconstruction of the correlation functions (2pt, 3pt and FH). In addition to plotting the corresponding posterior contribution from each class of excited state, we plot two hatched bands. The white hatched band is the sum of the 3pt sc and 2pt es contributions, which are observed to largely cancel, as indicated in Eq. (10). The gray hatched band is the sum of all excited state contributions (the full posterior distribution, minus the ground state, normalized by the ground state). The 3pt sc contribution is positive for $R_{A_3}(t_{\text{sep}}, \tau)$ and it becomes negative for $\text{FH}_{A_3}(t_{\text{sep}}, \tau_c = 1)$ at $t_{\text{sep}} > 0.5$ fm. The opposite is true for the 2pt es contribution. The sum of the scattering and two-point excited state contributions is opposite in sign to the transition excited state contributions, unlike for $R_{A_3}(t_{\text{sep}}, \tau)$ in which they are the same sign, leading to an even stronger suppression of the total excited state contributions beyond the expected suppression, as described in the text. The horizontal red dashed lines represent the threshold of a 1% contribution of excited state contamination to the ground state value.

to the 1% level by roughly 1 fm over a broad range of pion masses, $130 \lesssim m_\pi \lesssim 400$ MeV.

D. Comparison with late-time only results

In this section, we perform the correlator analysis on late time separation data, $t_{\text{sep}} = [10, 12, 14]$, which is directly comparable to the results in Refs. [24, 31] that were performed on the same ensembles, and otherwise mimicking the more common strategy used for example in Refs. [17, 21–23, 25, 26, 34].

The results are obtained with a simultaneous fit to the two- and three-point functions using the same priors as our main fit, given in App. B 1. We also demonstrate the sensitivity of the ground-state parameters posterior distributions to changes in the input priors as in App. B 2. Because we have only three values of t_{sep} , we use a minimal number of excited states: with one excited state, there is only one degree of freedom in describing the t_{sep} dependence of $R_\Gamma(t_{\text{sep}}, \tau)$, after which, the analysis relies upon the priors for the excited state matrix elements.

With the quark smearing we have used we have to apply a relatively aggressive truncation on the current insertion time in order for the model to describe the numerical data, restricting the analysis to the “center” of the current insertion time τ . We illustrate the region of τ used for each t_{sep} in Fig. 6 and depict the stability of the ground state axial matrix element in Fig. 7. The optimal result is chosen as the fit with the largest amount

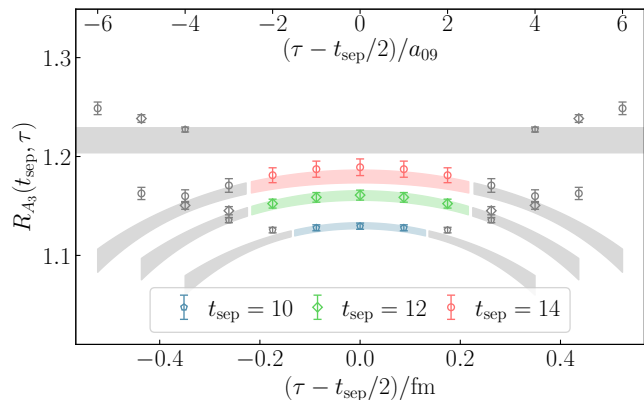


FIG. 6. We plot the numerical data for $R_{A_3}(t_{\text{sep}}, \tau)$ and resulting posterior fit bands obtained from a combined two-point and three-point analysis when only $t_{\text{sep}} = [10, 12, 14]$ are used in the analysis. The inner (colored) numerical data are used in the analysis. There is a break in the fit band and the outer (gray) band and data indicate regions of τ not used in the analysis. The horizontal gray band is the resulting posterior value of the ground state, \hat{g}_A .

of numerical data while maintaining a good fit quality (cfr. the lower panel of Fig. 7). We refer to the optimal choice of data included for this 2-state model fit as $\tau_{\text{inc}} = \tau_{\text{inc}}^{\text{opt}}$, but we also show results for the ground state posteriors when one more ($\tau_{\text{inc}}^{\text{opt}} + 1$) or one less ($\tau_{\text{inc}}^{\text{opt}} - 1$) value of τ is included in the fit. While not depicted, the

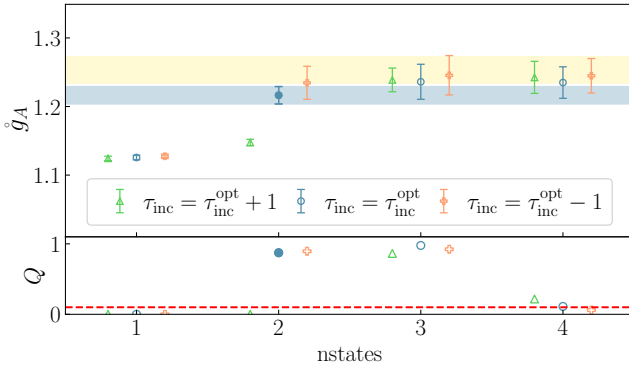


FIG. 7. The stability of \hat{g}_A versus the choice of current insertion times and number of states used in the analysis. The bottom panel shows the corresponding fit quality Q . The dark horizontal band indicates the optimal fit from the late- t_{sep} only analysis while the light horizontal band above it represent the optimal fit from the full analysis presented in Sec. III A.

ground state posteriors are also stable under variation of the choice of $t_{\text{sep}}^{\text{min}}$ in the two-point function.

We observe that for this specific dataset, the late- t_{sep} result is in $\approx 2\sigma$ tension with the result from the full analysis that includes much earlier values of t_{sep} . This is indicative that late- t_{sep} data can be subject to correlated fluctuations which are difficult to identify without having results at smaller values of t_{sep} which can point out the trend.

The same systematic effect can be seen in a simpler case using a fit to the two-point correlation function. In Fig. 8, we show the result of the ground state energy extracted from the two-point correlation function under varying $t_{\text{sep}}^{\text{min}}$. We highlight the best fit ground-state energy, which is supported by a robust plateau in the dimension of $t_{\text{sep}}^{\text{min}}$ with high Q -value. However, we see that at late time beyond 1 fm, a second plateau develops approximately two standard deviation above our best fit. Also note that we observe the fluctuation in the effective mass occur approximately 0.2 fm later than the matrix elements, see the top panel of Fig. 11 in App. B. This second “stable” plateau is also the logical result for a one-state fit. Analogous to the three-point analysis, if the model is insufficient at describing excited-state contaminations, the model must extract ground-state parameters at late time. These values are then sensitive to uncontrolled statistical fluctuations. Similar to the three-point analysis, in the absence of a more holistic view as granted by analyzing more source-sink separation data, there is no measure on the size of how large the potential underestimation of errors are.

Without using more than three values of t_{sep} , it is not possible to identify if one is susceptible to such a fluctuation, and therefore, it is not possible to fully quantify the uncertainty on the posterior distribution of the ground state parameters.

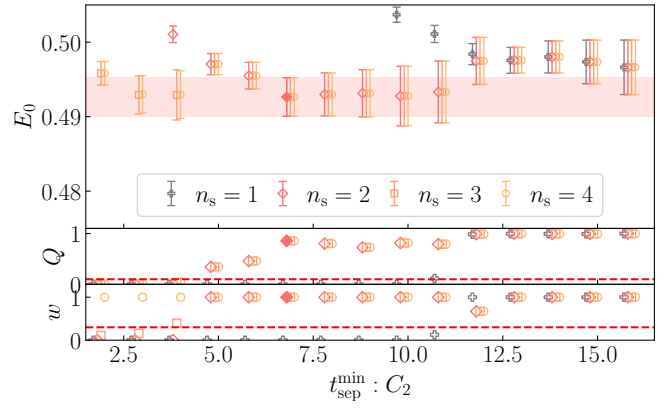


FIG. 8. The extracted ground state energy as a function of $t_{\text{sep}}^{\text{min}}$ and the number of states (n_s) used in the analysis. The late- t_{sep} data is subject to a correlated fluctuation, as observed in the 2σ increase in E_0 around $t_{\text{sep}}^{\text{min}} = 12$.

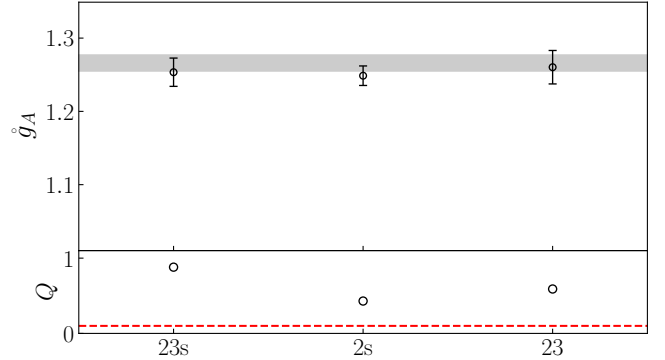


FIG. 9. Comparison of \hat{g}_A determined from the three analysis strategies described in the text with our result from Ref. [28] which utilized the Feynman-Hellmann correlator with a sum over all current insertion times [45].

E. Comparison with the 2-state FH analysis

In this final section, we compare our result with that from Ref. [28] on the same a09m310 ensemble. Those results were obtained using the Feynman-Hellmann method as described in Ref. [45], which is the same as Eq. (14) with the sum over current insertion time running over the full time extent, which includes contributions from contact operators at $\tau \in \{0, t_{\text{sep}}\}$ and from out-of-time region, $\tau < 0$ and/or $\tau > t_{\text{sep}}$. A two-state model and a frequentist analysis were used on the data from the two-point and Feynman-Hellmann correlation functions.

In Fig. 9 we show the extracted value of \hat{g}_A with three different fully-correlated analysis strategies:

23s : Fit to $C_2(t_{\text{sep}})$, $R_\Gamma(t_{\text{sep}}, \tau)$ and $\text{FH}_\Gamma(t_{\text{sep}}, \tau_c = 1)$;

2s : Fit to $C_2(t_{\text{sep}})$ and $\text{FH}_\Gamma(t_{\text{sep}}, \tau_c = 1)$;

23 : Fit to $C_2(t_{\text{sep}})$ and $R_\Gamma(t_{\text{sep}}, \tau)$.

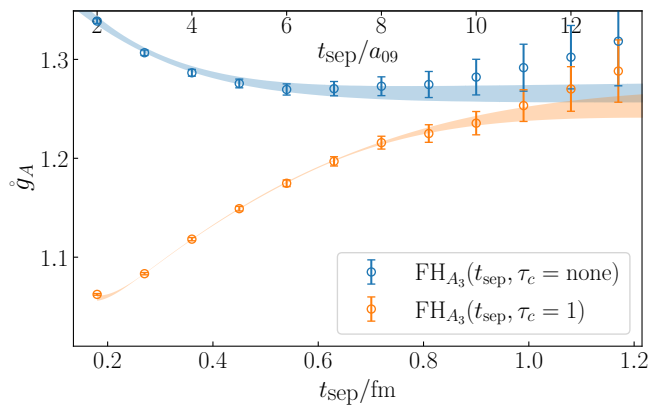


FIG. 10. Comparison of our $\text{FH}_{A_3}(t_{\text{sep}}, \tau_c = \text{none})$ numerical results and analysis from Ref. [28] using a two-state frequentist analysis (top data/band) to the $\text{FH}_{A_3}(t_{\text{sep}}, \tau_c = 1)$ numerical data and posterior description of the correlation function from the fully-correlated five-state Bayesian analysis to $C_2(t_{\text{sep}})$, $\text{FH}_{\Gamma}(t_{\text{sep}}, \tau_c = 1)$ and $R_{\Gamma}(t_{\text{sep}}, \tau)$ in the present work (bottom data/band).

The horizontal gray band is the result from Ref. [28]. These results show the consistency between the four computational and analysis strategies. Even though the $\text{FH}_{\Gamma}(t_{\text{sep}}, \tau_c)$ correlation functions are constructed from the $R_{\Gamma}(t_{\text{sep}}, \tau)$ correlation functions, they are subject to a different pattern of excited state contamination (cf. Sec. II). Therefore it is useful to include them in the fully-correlated analysis. The combined fit yields both a robust and consistent fitting strategy while also yielding precise extractions of hadronic matrix elements at zero-momentum transfer. Whether an analogous strategy can be pursued for non-zero momentum transfer is left for future work.

In Fig. 10, we present the posterior correlation function on top of the numerical data for both the results in Ref. [28] as well as from the $\text{FH}_{A_3}(t_{\text{sep}}, \tau_c = 1)$ dataset in the present work. The $\text{FH}_{A_3}(t_{\text{sep}}, \tau_c = \text{none})$ dataset from Ref. [28] is observed to have significantly less excited state contamination at early t_{sep} as compared to $\text{FH}_{A_3}(t_{\text{sep}}, \tau_c = 1)$. This is what enabled a two-state analysis in Ref. [28]. The combined fit (23s) in the present work enables a determination of significantly more excited state parameters through the precise early- t_{sep} data. Moreover, as shown in this section, a confident extraction of the ground state posterior distributions is attained: as depicted in the figure, both strategies yield precise and consistent extractions of the large- t_{sep} extrapolation of the results. The former result is more economical for obtaining a precise value of \hat{g}_A , while the method in this work also enables a determination of non-zero momentum transfer results which can be used to determine the form factors.

IV. OBSERVATIONS AND CONCLUSIONS

In this work, we have computed the three-point correlation functions that are used to determine the nucleon axial charge for 13 values of the source-sink separation time in the range $t_{\text{sep}} \approx 0.17 - 1.22$ fm on an ensemble with $a \approx 0.09$ fm and $M_{\pi} \approx 310$ MeV. This large numerical dataset (Fig. 1) has enabled us to robustly determine the ground state mass and matrix elements with a fully-quantified systematic uncertainty arising from excited states. It further enabled us to quantify the excited state contribution to the correlation function with greater detail than has been previously achieved in the literature. We were able to demonstrate that the ground state parameters are stable against the model of excited states (Eq. (16) and Fig. 3), the number of excited states used in the analysis, and truncations of either small t_{sep} or large t_{sep} results as well as through the use of only even or odd values of t_{sep} results (Fig. 4).

A re-writing of the spectral decomposition of the three-point correlation functions revealed a prospective cancellation between two classes of excited states arising from the n -to- n scattering states and those arising from the two-point correlation function used to construct $R_{\Gamma}(t_{\text{sep}}, \tau)$, Eq. (10) (there is an exact cancellation for the vector matrix element for which $g_{nn}^{V_4} = g_{00}^{V_4} = 1$ up to renormalization). For our calculation, this cancellation seems to materialize for g_A (Fig. 5) leaving the dominant excited state contributions to be the n -to- m transition terms. In the standard fixed source-sink separation method, the excited state contributions do not decay down to the 1% contamination level until $t_{\text{sep}} \gtrsim 2$ fm while in the Feynman-Hellmann correlation function, Eq. (14), they decay to the 1% level at $t_{\text{sep}} \approx 1$ fm. We further observed that the Feynman-Hellmann correlation function constructed with a sum over the entire time extent of the lattice [45] ($\text{FH}_{\Gamma}(t_{\text{sep}}, \tau_c = \text{none})$), rather than just between the source and the sink ($\text{FH}_{\Gamma}(t_{\text{sep}}, \tau_c = 1)$), leads to an even further suppression of excited state contamination (Fig. 10). This stronger cancellation of excited states is what enabled us to compute g_A with a $\approx 1\%$ uncertainty by utilizing early-time data [27–30], which demonstrated this higher suppression of excited states over a broad range of pion masses, $130 \lesssim m_{\pi} \lesssim 400$ MeV.

By utilizing a large number of early to mid-time data, one is able to detect if the late-time data is subject to a correlated fluctuation which might otherwise bias the ground state matrix elements (Figs. 7 and 8). With only three values of t_{sep} at late time, it is not possible to perform such a data truncation study that could identify this issue. We have found that, even though the Feynman-Hellmann correlation functions, which are constructed from the three-point functions as in Eq. (14), are highly correlated with $R_{\Gamma}(t_{\text{sep}}, \tau)$, including them in a global fully-correlated analysis improves the stability and precision of the extracted ground state parameters (Fig. 9) as the excited states present themselves differently in the

two sets of matrix-element correlation functions.

Due to the exponential degradation of the signal-to-noise of the nucleon’s two- and three-point correlation functions as t_{sep} is increased, which requires exponentially more computational resources to control the stochastic precision, the strategy we present in this work offers a more economical method of obtaining the ground state matrix elements than that which is more commonly advocated for in the literature, which is to use high-statistics calculations at $t_{\text{sep}} \approx 1 - 2$ fm or larger. In future work, we will investigate the same strategy for non-zero momentum transfer correlation functions which are used to determine the nucleon form factors.

Data availability: The computations were performed utilizing LaLiBe [91] which utilizes the Chroma software suite [84] with QUDA solvers [92, 93] and HDF5 [94] for I/O [95]. They were efficiently managed with METAQ [96, 97] and status of tasks logged with EspressoDB [98]. The final extrapolation analysis utilized gvar [99] and lsqfit [100]. The analysis and data for this work can be found at https://github.com/callat-qcd/project_fh_vs_3pt.

ACKNOWLEDGMENTS

We thank O. Bär, R. Briceño, M. Hansen and A. Jackura for enlightening conversations and correspondence. We thank B. Hörz for help cross-checking the three-point code in LaLiBe and generating some of the results. We thank the MILC Collaboration for use of their HISQ gauge ensembles.

Computing time for this work was provided through the Innovative and Novel Computational Impact on Theory and Experiment (INCITE) program and the LLNL Multiprogrammatic and Institutional Computing program for Grand Challenge allocations on the LLNL supercomputers. This research utilized the NVIDIA GPU-accelerated Summit supercomputer at Oak Ridge Leadership Computing Facility at the Oak Ridge National Laboratory, which is supported by the Office of Science of the U.S. Department of Energy under Contract No. DE-AC05-00OR22725 as well as the Lassen supercomputer at Lawrence Livermore National Laboratory.

This work was supported in part by the NVIDIA Corporation (MAC), the Alexander von Humboldt Foundation through a Feodor Lynen Research Fellowship (CK), the DFG and the NSFC Sino-German CRC110 (EB), the RIKEN Special Postdoctoral Researcher Program (ER), the U.S. Department of Energy, Office of Science, Office of Nuclear Physics under Award Numbers DE-AC02-05CH11231 (CCC, CK, BH, AWL), DE-AC52-07NA27344 (DAB, DH, ASG, PV), DE-FG02-93ER-40762 (EB), DE-AC05-06OR23177 (CJM); DE-SC00046548 (AN); the Berkeley Laboratory Undergraduate Research Program (IC); the U.K. Science and Technology Facilities Council grants ST/S005781/1 and

ST/T000945/1 (CB); and the DOE Early Career Award Program (AWL).

Appendix A: Discrete symmetry systematics

“*Coherent sink technique*” [10]: We reduce the numerical cost of the computations by solving for a single sequential-propagator from many sequential sinks simultaneously. We found that we can combine eight sinks into a single coherent sink generated with two sources per timeslice, with a 10-20% loss in statistical precision as compared to solving a single sequential-propagator for each of the eight sources separately. For each t_0 , a random origin (O) is chosen and then the anti-pode (A) location is also chosen [101]

$$s_{\text{O}}(t_0) = (x_0, y_0, z_0)$$

$$s_{\text{A}}(t_0) = \left[s_{\text{O}}(t_0) + \frac{L}{2}(1, 1, 1) \right] \bmod L.$$

We repeat this for four values of t_0 spaced by $T/4$. We generate all 16 sources by running a second set of eight sources shifted by $T/8$ from the first set of sources.

Spin-averaging: We find that combining the spin-up-to-spin-up and spin-down-to-spin-down correlation functions (with a + sign for V_4 and a - sign for A_3) leads to a near perfect $\sqrt{2}$ reduction in the stochastic uncertainty of the numerical data. We further observe that the non-symmetric behavior of $R_{\Gamma}(t_{\text{sep}}, \tau)$ about $\tau = t_{\text{sep}}/2$ for larger values of t_{sep} , which must vanish in the infinite statistics limit, are less pronounced when we perform this spin-averaging.

Time-reversal symmetry: We find that combining the backwards temporal propagation of the negative-parity two- and three-point functions – the time-reversed correlation functions (negative parity three-point functions with negative values of the source-sink separation time $t_{\text{sep}} = t_{\text{snk}} - t_{\text{src}} < 0$) with the positive parity three-point functions generated with $t_{\text{sep}} > 0$ leads to a near-perfect $\sqrt{2}$ reduction in stochastic uncertainty, allowing us to make use of both the positive and negative parity components of the quark propagators.

Appendix B: Analysis Details

In this appendix, we discuss in detail the analysis of the various correlation functions and what led us to our final strategy presented in Sec. III.

To analyze the two-point (2pt), Eq. (1), three-point (3pt), Eq. (6) and Feynman-Hellmann (FH), Eq. (14) correlation functions and determine the parameters of the fit model, we perform a multi-exponential Bayesian analysis. We explore analyzing three combinations of correlation functions in a global (simultaneous) analysis:

$$\mathbf{23s} : C_2(t_{\text{sep}}), R_{\Gamma}(t_{\text{sep}}, \tau) \text{ and } \text{FH}_{\Gamma}(t_{\text{sep}}, \tau_c = 1);$$

2s : $C_2(t_{\text{sep}})$ and $\text{FH}_\Gamma(t_{\text{sep}}, \tau_c = 1)$;

23 : $C_2(t_{\text{sep}})$ and $R_\Gamma(t_{\text{sep}}, \tau)$.

1. Prior selection

The first step in the analysis is to choose prior distributions for the parameters. In order to estimate the ground state priors, we use the effective mass, the effective overlap and an effective g_A plot:⁷

$$\begin{aligned} m_{\text{eff}}(t_{\text{sep}}) &= \ln \left(\frac{C_2(t_{\text{sep}})}{C_2(t_{\text{sep}} + 1)} \right), \\ z_{\text{eff}}^2(t_{\text{sep}}) &= e^{m_{\text{eff}}(t_{\text{sep}})t_{\text{sep}}} C_2(t_{\text{sep}}), \\ g_A^{\text{eff}} &= \text{FH}_{A_3}(t_{\text{sep}}, \tau_c = 1). \end{aligned} \quad (\text{B1})$$

In Fig. 11, we plot these effective quantities which all asymptote to their ground state values in the large t_{sep} limit. We choose conservative ground state priors to be

$$\begin{aligned} \tilde{E}_0 &= 0.50(5), & \tilde{g}_A &= 1.2(2), \\ \tilde{z}_0 &= 0.00034(34), & \tilde{g}_V &= 1.0(2), \end{aligned} \quad (\text{B2})$$

which are plotted as the wide gray horizontal bands. We also plot the resulting posterior distribution of the effective parameter correlation functions resulting from our final analysis.

For the excited state energies we explore three models of excited states, Eq. (16). As shown in Fig. 3, the posterior energies are largely insensitive to the model. We therefore focus the discussion on the spectrum of our chosen model, $\Delta E_n = 2m_\pi$ for all n . The lowest-lying excitation is a nucleon-pion P-wave or a nucleon with two-pions at rest, up to interaction energies which are a small fraction of the total energy. For our $m_\pi L$, these two energy levels are practically degenerate and therefore modeled as a single excitation. We prior all the ΔE_n with a log-normal distribution, $\ln(\Delta E_n) = (\ln(2m_\pi), 0.5)$ such that the resulting energies, $E_n = E_0 + \sum_{l=1}^n \Delta E_l$ are ordered.

While the creation and annihilation operators are conjugate to each other, this does not fix the absolute sign of z_n . Further, there is a redundancy in sign of the transition matrix elements: if all the overlap factors are taken to be positive, $z_n > 0$, a negative contribution will manifest in a negative value of g_{nm} . Only the combination $z_n z_m^\dagger g_{nm}$ has a well defined sign.

To be conservative, we prior the central values of the excited state overlap factors with a central value of 0. For the first excited state, we chose a slightly smaller prior width with respect to the ground state and for the higher excited states, use use agagin a slightly smaller width:

$$\tilde{z}_1 = 0(0.00025), \quad \tilde{z}_{n \geq 2} = 0(0.00015). \quad (\text{B3})$$

⁷ We do not show the effective g_V plot since with our action, g_V is very close to 1.

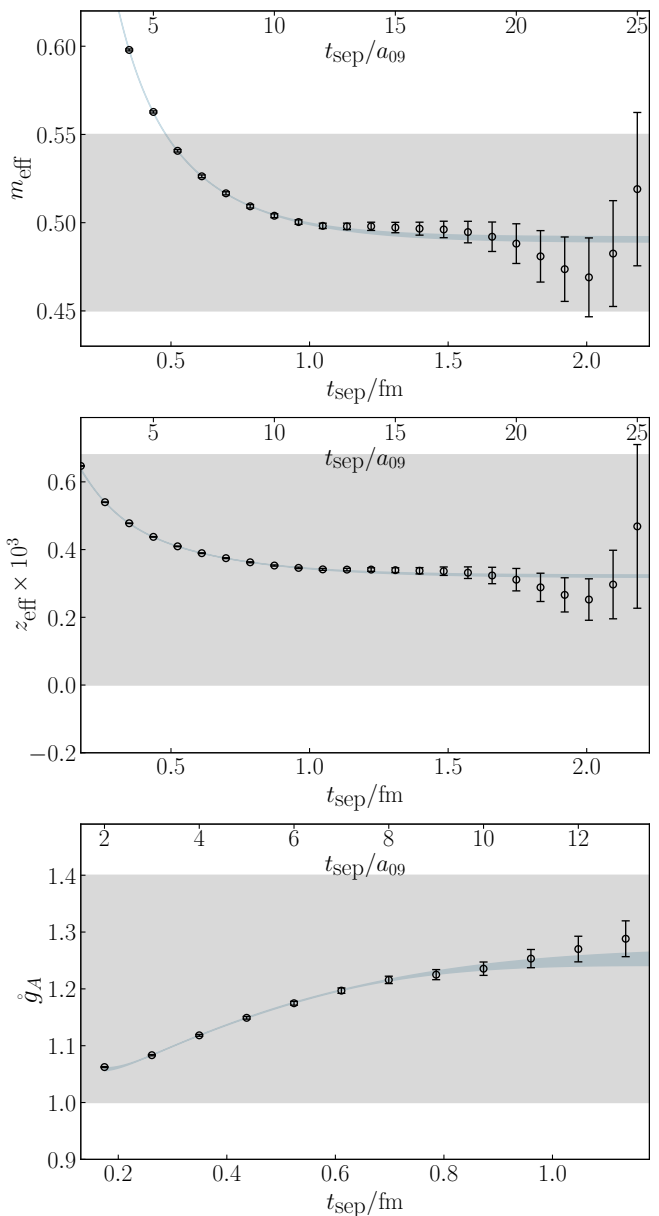


FIG. 11. The effective mass (Top), overlap factor (Middle) and g_A correlation functions (Bottom). The wide horizontal gray bands are the chosen ground state priors, while the blue overlay bands are the reconstructed effective quantities using the posterior distributions from the final analysis.

These slight reductions are motivated by the use of a smeared quark source, which suppresses excited state overlap factors compared to the ground state.

For the vector matrix elements, the conserved charge protects the charge of all states to be $g_{nn}^V = 1$, even in finite volume [90]. For the transition matrix elements, we postulate that these are the same order of magnitude, but with an unknown sign. For the axial-vector matrix elements, we postulate the excited state matrix elements and transition matrix elements are of the same order

of magnitude as g_A . This leads us to the prior values of

$$\begin{aligned} g_{nn}^V &= 1.0(2), & g_{nn}^A &= 1.2(2), \\ g_{nm}^V &= 0(1), & g_{nm}^A &= 0(1). \end{aligned} \quad (\text{B4})$$

A complete list of the prior, and posterior distributions of all fit parameters is provided in App. C.

When performing a multi-exponential fit, it is expected that the highest state used in the analysis serves as a “garbage” can that is contaminated by the tower of more highly-excited states not included in the analysis. The 3pt and FH correlation functions have different parametric dependence upon the excited states. Therefore, when exploring the parameter space of fits, if the number of states used for example in the FH correlation functions differs from the 2pt function, we allow the highest lying state in each correlation function to have different priors. Specifically, if the 2pt uses five states and the FH uses three-states, then the energy and overlap priors of the third FH state are decoupled from the third state of the 2pt function. When the number of states used is the same, we find we are able to describe the correlation functions well when keeping the highest garbage-can state the same in all correlation functions.

2. Sensitivity analysis

For each set of correlation functions, the best fit is chosen after a careful study of the posterior distribution sensitivity on input fit parameters including fit ranges, number of states in the fit model, prior widths, and model dependence of the excited state spectrum. In the following sections, we discuss the best fit under the context of three different fit strategies, **23**, **2s** and **23s**, and then the costs and benefits of these different strategies.

a. Fit region and n_{state} stability analysis

Due to the structure of excited state contamination, the posterior distributions are most sensitive to changes in $t_{\text{sep}}^{\text{min}}$, the minimum source-sink time, and the number of excited states chosen in the model. In this section we discuss the stability of the best fit under changing inputs to these two dimensions.

Two-point with Feynman-Hellmann analysis (2s)

Fig. 12 shows the dependence on the axial-vector matrix element fit parameter, \hat{g}_A , under varying two-point and FH $t_{\text{sep}}^{\text{min}}$, and their corresponding n_{states} . Typically, stability plots demonstrate that the best fit lies at a locally optimal point in the parameter space. The simplest strategy is to simply fix all but one parameter, such as $t_{\text{sep}}^{\text{min}}$ or n_{states} in this section. If results surrounding the best fit are absent of spurious correlations, then the stability plots provide evidence that systematic errors arising from the fit procedure are all accounted for. However,

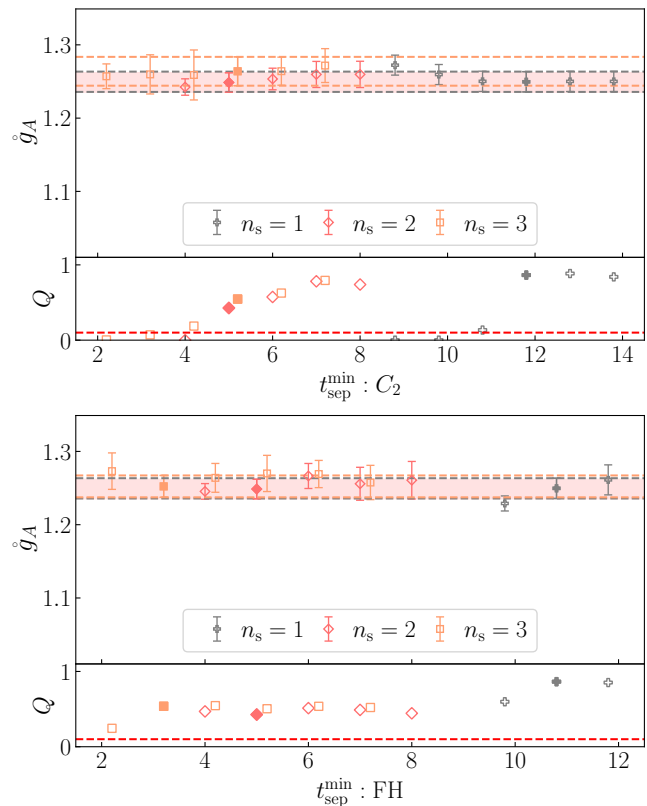


FIG. 12. Stability analysis for the axial coupling for the combined two-point and Feynman-Hellmann fit for (Top) varying t_{min} of the two-point function and (Bottom) Feynman-Hellmann correlation function. In both cases, results of $n_s = [1, 2, 3]$ state fit ansatzes are shown. The best fit for a given n_s is highlighted by a solid marker and corresponding horizontal band. The filled horizontal red band for the $n_s = 2$ result highlights the best fit out of the entire explored parameter space. The corresponding Q -values are also provided.

in the case of the FH form of the correlation function, the time dependence observed is analogous to a two-point correlation function. And similar to the two-point function, the best fit for a given number of excited states, requires a more careful choice of $t_{\text{sep}}^{\text{min}}$. For example, a two-point fit with many excited states may successfully describe the data at small source-sink separation times, but will surely fail when the model is simplified. Therefore, for the stability plots shown in Fig. 12, the analysis varies $t_{\text{sep}}^{\text{min}}$ around the best fit for a given number of states in the model. For simplicity, we vary the $t_{\text{sep}}^{\text{min}}$ of the vector and axial-vector matrix elements in tandem.

After the summation, the three-point correlation function only has one degree of freedom per time slice. Coupled with the fact that the signal-to-noise is exponentially worse compared to the two-point (see Fig. 11), means that in order to prevent over-fitting the data, simpler fit models with less excited states should be chosen. Therefore, the stability shown in Fig. 12 is checked for fits with 1, 2, and 3 states. Beyond three states, the model will

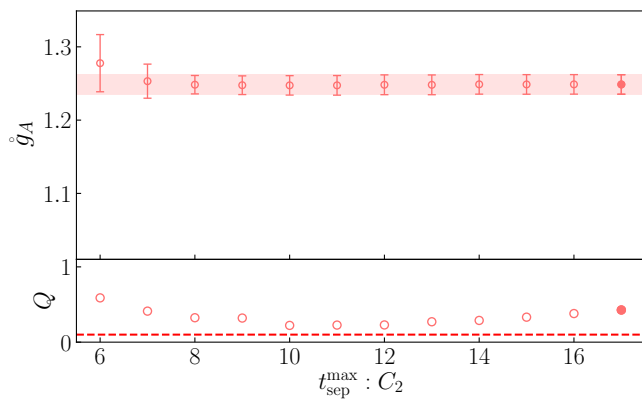


FIG. 13. Stability analysis for the axial coupling for the combined two-point and Feynman-Hellmann fit for varying t_{\max} of the two-point function. The best fit highlighted by a solid marker and corresponding horizontal band is identical to the one shown in Fig. 12. The corresponding Q -values are provided.

have comparable or more parameters than data. While this can in principle be alleviated with careful choices of priors, strategies that rely more heavily on prior information may also inadvertently introduce possible systematic errors.

For a single state, we observe the fit to be stable at approximately a source-sink separation time of 1 fm and identifies the length scale in which all excited-states have decayed to below the noise given a percent-level determination of the matrix element. This observation is consistent with what is observed in our previous work [28, 45]. With two and three state fits, we observe that the best fit t_{sep}^{\min} can encompass progressively shorter source-sink separation times, in agreement with expectation. Furthermore, the best fit for the three models, and neighboring results, are all consistent within one standard deviation with no appreciable systematic trend.

A two-state fit allows us to capture some of the excited state dependence in order to not rely entirely on the correlator reaching the plateau region. Simultaneously, fitting to two states avoids the possibility of over-fitting since an introduction of three additional fit parameters (ground state and first excited state matrix elements) can be extracted from 10 data points in this specific analysis (t_{sep}^{\min} of 5 to 14). We assume that the overlap and energies are well constrained by the two-point correlation function in this counting. The three-state fit introduces 6 new matrix element parameters, and is at the edge of what is naively allowed by data. Fitting to three states allows t_{sep}^{\min} to encompass down to $t_{\text{sep}} = 4$, resulting in 12 data points. However, since lattice correlation functions have an exponential signal-to-noise problem, data points do not carry equal weight in determining the posterior distributions. In particular, the weighted loss function penalizes larger time separation data with the inverse of the variance. Referring back to Fig. 11, we see for this

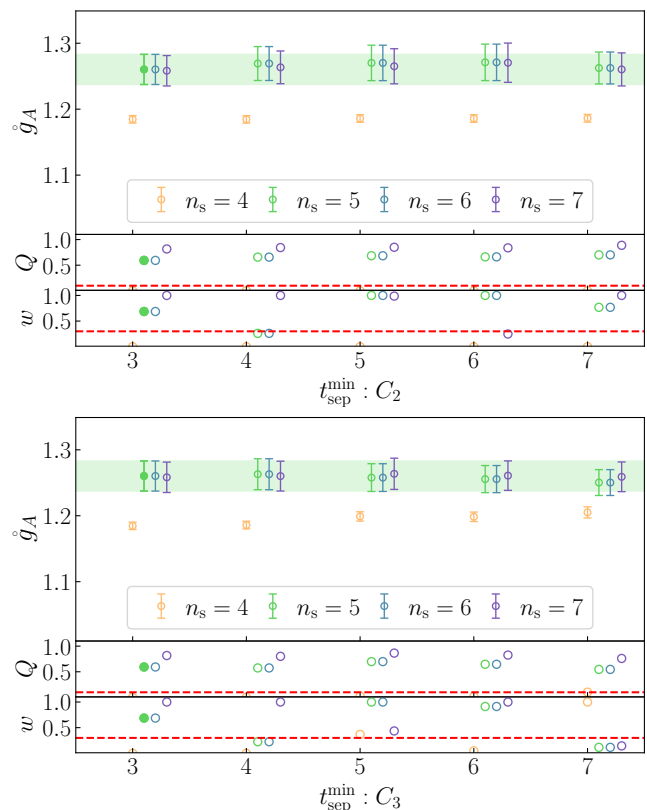


FIG. 14. Stability analysis for \hat{g}_A for the combined two-point and three-point fit for (Top) varying t_{\min} of the two-point function and (Bottom) three-point correlation function. In both cases, results of $n_s = [4, 5, 6, 7]$ state fit ansatzes are shown. The filled marker and horizontal green band for the $n_s = 5$ result highlights the best fit. The corresponding Q -values are provided. The Bayes Factors for a given t_{\min} are shown at the bottom panel of each plot labelled w .

specific example, data beyond t of 9 have little impact on the outcome of the result. This can be seen for example in Fig. 13 where the results are given for varying t_{\max} of the two-point function. As a result, the three state fit with 6 extra parameters is effectively constrained by approximately 6 data points. It follows that more complicated fit functions run into the danger of over-fitting. We conclude that fits to the FH correlation function are best performed with two states.

Two-point with three-point analysis (23)

Rather than constructing the FH combination, we explore the possibility of fitting directly to the three-point correlator as a function of both source-sink and current-sink insertion time. Due to the complexity involved in choosing a two-dimensional fit region, we simplify the decision making process by fitting to all valid insertion-sink time separation times (the contact terms are dropped) as shown in Fig. 15. This choice reduces the t_{sep}^{\min} stability study to again a single dimension. To capture this

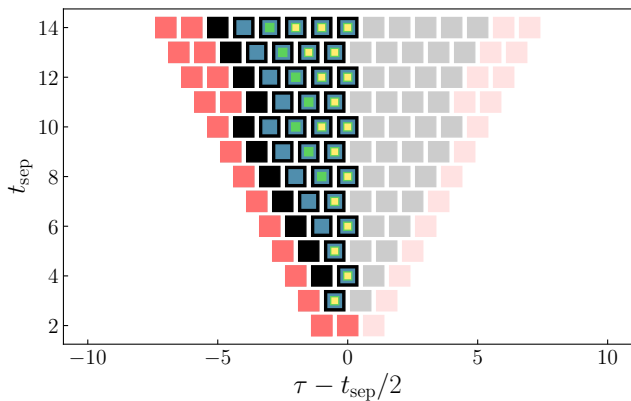


FIG. 15. This figure depicts the regions in t_{sep} and τ used in the analysis. The numerical results have been averaged about $\tau = t_{\text{sep}}/2$ denoted by the light-shaded squares on the right half of the figure. The outer-most (red) squares for each t_{sep} are the points $\tau = 0$ or $\tau = t_{\text{sep}}$ which are excluded from the analysis. For $t_{\text{sep}} > 10$, the values of $\tau = 1$ and $\tau = t_{\text{sep}} - 1$ are also excluded from the optimal fit. Moving in, the (black) squares represent the values of τ closest to the source/sink times included in the optimal analysis (with all “inner” values of τ also included), $\tau_{\text{inc}}^{\text{opt}}$. Cutting an additional value of τ closest to the source/sink times is $\tau_{\text{inc}}^{\text{opt}} - 1$ denoted by the lighter (blue) squares. The lighter (green) squares denote $\tau_{\text{inc}}^{\text{opt}} - 2$ and the innermost (yellow) squares denote $\tau_{\text{inc}}^{\text{opt}} - 3$. When cutting values of τ , we always keep one (for even t_{sep}) or two (for odd t_{sep}) values of τ in the middle of the source-sink separation time.

curvature, a large number of excited states are required. However, unlike the FH correlator, the three-point correlator supplies many data points as shown in Fig. ??, and can be used to fully capture the complicated excited-state structure. Additionally, conservative smearing on the interpolating operator yields a two-point correlator that provides corroborating support to a large number of excited states when fit to small source-sink separation times. Due to the large number of states, stability with respect to $t_{\text{sep}}^{\text{min}}$ are less sensitive to n_{states} . As a result, we further simplify the study by showing only stability with respect to the final result, instead of first identifying n_{states} -dependent best fits shown in Fig. 12.

Fig. 14 shows the stability of the best fit for the two-point and three-point simultaneous fit under varying $t_{\text{sep}}^{\text{min}}$ for the two-point and three-point function. Similar to the FH fit in the previous section, we simplify the analysis by varying the $t_{\text{sep}}^{\text{min}}$ for the vector and axial-vector matrix elements simultaneously. The best fit presumably can be slightly improved if this condition is relaxed. Due to the choice of fitting all current insertion times (aside from the source and sink time), the best fit is observed to require a 5 state model, and includes source-sink separation times that are commensurate to the inclusion of small insertion-sink times. The best fit lies in the region of stability, and is chosen to incorporate the most data possible given a fit model. Alternatively, given a fit

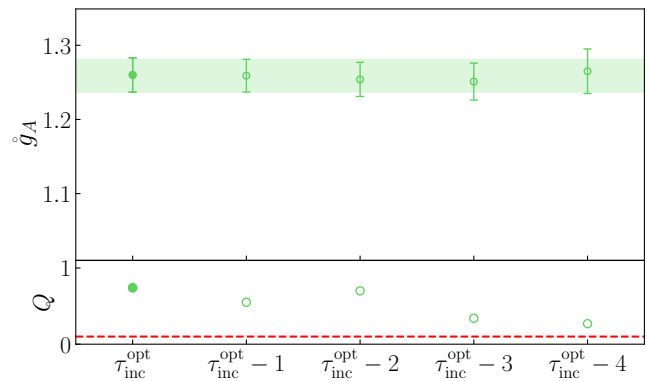


FIG. 16. Stability analysis for the combined $C_2(t_{\text{sep}})$ and $R_{\Gamma}(t_{\text{sep}}, \tau)$ analysis for varying regions of current-insertion time. The best fit given by $\tau_{\text{inc}}^{\text{opt}}$ is defined in Table III (see also Fig. 15 for a graphical depiction of $\tau_{\text{inc}}^{\text{opt}} - n$). The filled marker and horizontal green band highlights the best fit and is identical to the best fit in Fig. 14. The Q -values are provided.

region, the simplest model is chosen (fewest number of states). For example, the best fit with a three-point $t_{\text{sep}}^{\text{min}}$ of 3 includes 5 states even though 6 or 7 states yields similar ground state posterior distributions. This decision is corroborated with the set of Bayes factors normalized to a fixed fit region. For example, Fig. 14 suggests that 5 state and 7 state fit have comparable probability for reproducing the underlying data.

While we make the choice of fitting data over all current insertion times, the ground-state posterior distributions are stable when extracted from a subset of the data. In Fig. 16, the fit region with respect to current insertion time is symmetrically truncated, keeping however, at least one data point per source-sink separation time (*e.g.* $t_{\text{sep}} = 3$ includes $\tau = [1, 2]$, so a $\tau_c = 1$ will not eliminate any data since otherwise the entire dataset for $t = 3$ would be eliminated). It is also observed that while curvature in τ is dependent predominantly on excited-state behavior, aggressively truncating data still leads to larger statistical uncertainty in ground state parameters since less data is being included in the analysis.

We conclude that a simultaneous fit to the two- and three-point correlators is best performed by fitting to the maximum amount of data while choosing the simplest model which can describe the data. In particular, we observe that the under this strategy, the accompany two-point correlator also provides sufficient constraints on the excited state overlap and energy parameters.

Two-point, three-point and FH Analysis (23s)

Finally, we perform a simultaneous fit to the two-point correlator along with all FH and three-point correlators. Since the FH correlator exposes different excited-state dependence when compared to the three-point correlator, it may be possible to extract a more robust calculation of the ground state parameters. Unfortunately, the

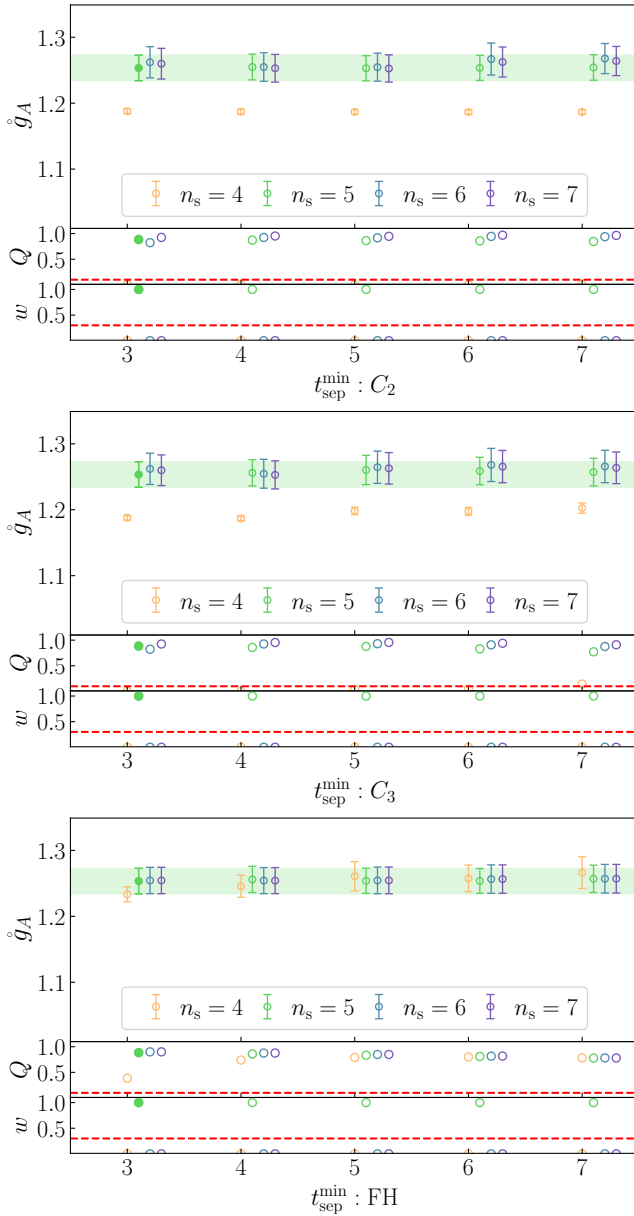


FIG. 17. Stability analysis for the combined two-point, three-point, and Feynman-Hellmann analysis. These plots follow what is shown in Fig. 14.

overall strategy of the previous two studies are incompatible with one another. In the case of the FH analysis, the strategy is to fit simpler models in order to avoid overfitting, while for the three-point analysis overfitting is much less of a concern and instead a majority of clean data is fitted with more complex models. A successful combined fit will need to reconcile these differences.

We take a simple approach by recognizing that the excited state information extracted from the three-point analysis can be used to constrain a more complex FH fit function. Following this logic, the best combined fit follows the same 5 state model as the two-point with

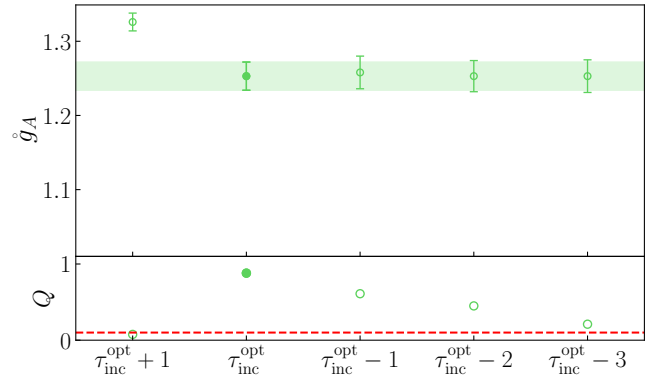


FIG. 18. Stability analysis for the combined two-point, three-point, and Feynman-Hellmann analysis for varying regions of current-insertion time. This plot follows what is shown in Fig. 16.

three-point correlator fit discussed previously, while the FH fit is now modelled by 5 states with the intention of relying on the three-point correlator to constrain high excited state parameters. Fig. 17 demonstrates the stability of the combined best fit under changes in $t_{\text{sep}}^{\text{min}}$ of the two-point, three-point and FH correlators. We observe that in the combined fit the ground-state parameters are insensitive to changes in $t_{\text{sep}}^{\text{min}}$ for all datasets, including the FH correlation functions. This observation lends evidence to the hypothesis that the three-point correlator lends support to high excited-state contributions which is consistent with the predicted spectral decomposition for both correlation functions. Additionally, while the best fit $t_{\text{sep}}^{\text{min}}$ for the three-point is kept the same as the three-point with two-point fit, the best-fit FH $t_{\text{sep}}^{\text{min}}$ is now extends down to $t_{\text{sep}} = 3$ (where previously in the 2 state fit the best fit $t_{\text{sep}}^{\text{min}}$ is 5) due to the inclusion of more states in the model.

Finally, sensitivity under varying current insertion time for the three-point correlator is studied. Unlike the simpler three-point with two-point correlator analysis, we have to drop one additional data point away from the contact interaction at $t = 11$ to $t = 14$ for the ground-state posterior distributions to be insensitive to changes in fit region. Fig. 18 shows the varying fit region with respect to the best fit. In particular, the $\tau_{\text{inc}}^{\text{opt}} + 1$ fit is to all current insertion dependence between the source and sink, $\tau = [1, t_{\text{sep}} - 1]$ for all t_{sep} . The colored regions in Fig. 15 highlights the various τ_{inc} regions with the colored boxes. The black region denotes the best fit region. We observe that the best fit lies in a region that is insensitive to varying subsets of the three-point correlator. Conversely, the combined fit suggests that at large values of t_{sep} , where the distribution of the correlator become under-sampled, the three-point data shows signs of being inconsistent with the FH data, leading to the instability seen in $\tau_{\text{inc}}^{\text{opt}} + 1$ fit.

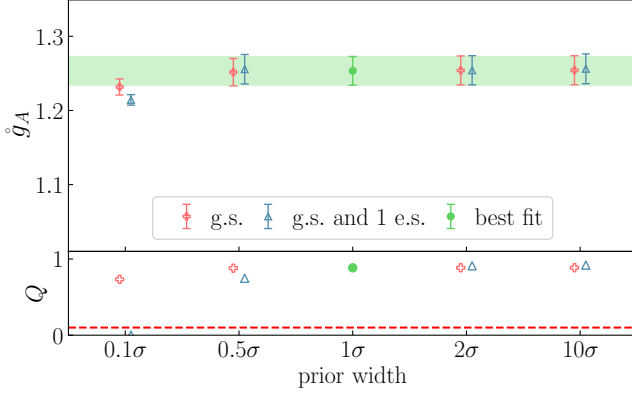


FIG. 19. Sensitivity analysis of the best fit result from the combined two-point, three-point, and Feynman-Hellmann fit under varying prior widths for the ground-state (red) and together with the first-excited state (blue). The x -axis indicates that the study performed variations from 0.1 to 10 times the best fit prior width. The filled marker and horizontal green band highlights the best fit and is identical to the result shown in Fig. 17.

We conclude that the three-point correlator provides enough information to constrain the excited-states of the FH correlator. A combined fit is therefore, best performed by rooting the calculation in a two-point with three-point strategy and extending the analysis to encompass as much of the FH correlator as is describable by the truncated spectral decomposition.

b. Prior width analysis

Our overall strategy is to extract ground-state parameters from a multi-exponential fit, subject to prior constraints. Since the objective function now depends on prior distributions in addition to data, we check that the posterior distributions of interest are insensitive to our prior knowledge. The purpose of introducing priors in this context is not to supplement additional information, but to constrain the search space of the numerical minimization for faster convergence. Lower computation costs allow us to explore more thoroughly investigate the sensitivity of ground state posterior distributions, which in turn leads to more robust results. It follows then, that we enforce the expectation that choices of priors should not yield changes in the posterior distributions of ground-state parameters.

Fig. 19 demonstrates the robustness of our quoted results under varying prior widths of the ground-state and first-excited state prior widths for the combined fit. The study indicates that the extracted matrix elements are unconstrained by prior distributions until the widths are

reduced by a factor of 10, while broadening the prior distribution by a factor of 10 leaves the matrix elements unchanged. Similar conclusions hold for the vector ma-

TABLE I. We list the prior and posterior energies and overlap factors, in lattice units, for each of the parameters determined that describe the two-point correlation function. The prior and posterior values are listed in (μ, σ) pairs. The energy splittings are priorred with a log-normal distribution with $\Delta E_n = (2m_\pi, m_\pi)$, except for the highest state which has a prior width of $5m_\pi$, with the total energy given by the sum in Eq. (16). For the optimal fit, all energy splittings are given a central value of $2m_\pi$.

| Parameter | Prior | Posterior |
|------------------|--------------------|------------------------|
| E_0 | (0.50, 0.05) | (0.4904, 0.0016) |
| $\Delta E_{n<4}$ | (0.29, 0.14) | (0.3, 0.028) |
| E_1 | (0.79, 0.15) | (0.79, 0.028) |
| E_2 | (1.07, 0.21) | (1.136, 0.099) |
| E_3 | (1.36, 0.25) | (1.66, 0.16) |
| ΔE_4 | (0.29, 0.72) | (1.119, 0.033) |
| E_4 | (1.65, 0.76) | (2.78, 0.16) |
| z_0 | (0.00034, 0.00034) | (0.0003211, 0.0000039) |
| z_1 | (0, 0.00025) | (0.000333, 0.000031) |
| z_2 | (0, 0.00015) | (-0.000331, 0.000062) |
| z_3 | (0, 0.00015) | (0.000617, 0.000034) |
| z_4 | (0, 0.00015) | (0.00032, 0.00011) |

TABLE II. Priors and posteriors of the vector and axial-vector matrix elements. The values are listed in (μ, σ) pairs.

| g_{nm}^A | Prior | Posterior | g_{nm}^V | Prior | Posterior |
|------------|------------|-----------------|------------|----------|--------------------|
| g_{00}^A | (1.2, 0.2) | (1.253, 0.019) | g_{00}^V | (1, 0.2) | (1.02238, 0.00087) |
| g_{01}^A | (0, 1) | (-0.271, 0.068) | g_{01}^V | (0, 1) | (-0.0041, 0.004) |
| g_{11}^A | (0, 1) | (0.89, 0.2) | g_{11}^V | (1, 0.2) | (0.997, 0.02) |
| g_{02}^A | (0, 1) | (-0.16, 0.11) | g_{02}^V | (0, 1) | (0.002, 0.013) |
| g_{12}^A | (0, 1) | (-0.05, 0.3) | g_{12}^V | (0, 1) | (0.013, 0.042) |
| g_{22}^A | (0, 1) | (0.71, 0.53) | g_{22}^V | (1, 0.2) | (1.05, 0.12) |
| g_{03}^A | (0, 1) | (0.1, 0.043) | g_{03}^V | (0, 1) | (0.0798, 0.0075) |
| g_{13}^A | (0, 1) | (0.14, 0.14) | g_{13}^V | (0, 1) | (0.071, 0.025) |
| g_{23}^A | (0, 1) | (0.25, 0.31) | g_{23}^V | (0, 1) | (-0.011, 0.062) |
| g_{33}^A | (0, 1) | (0.87, 0.22) | g_{33}^V | (1, 0.2) | (0.789, 0.047) |
| g_{04}^A | (0, 1) | (0.61, 0.21) | g_{04}^V | (0, 1) | (0.35, 0.12) |
| g_{14}^A | (0, 1) | (0.4, 0.25) | g_{14}^V | (0, 1) | (0.33, 0.13) |
| g_{24}^A | (0, 1) | (-1.06, 0.52) | g_{24}^V | (0, 1) | (-0.34, 0.16) |
| g_{34}^A | (0, 1) | (0.72, 0.39) | g_{34}^V | (0, 1) | (0.63, 0.24) |
| g_{44}^A | (0, 1) | (-0.32, 0.95) | g_{44}^V | (1, 0.2) | (1, 0.2) |

trix element for the two-point with sub-subtracted, and two-point with three-point strategies.

Appendix C: Prior and posterior distributions

In Table 17, we list the prior and posterior distributions of the energies and overlap factors used in our final analysis. The matrix element prior and posterior distributions are given in Table II. In Table III, we list the range of t_{sep} values used in the three sets of correlation functions that are analyzed.

TABLE III. We list the range of t_{sep} values used in our optimal fits for each of the three sets of correlation functions we analyze. We also list the values of the current insertion time, τ , for which the optimal fit uses $\tau = [1, t_{\text{sep}} - 1]$ for the **23** analysis (2pt and 3pt). When we perform the **23s** (2pt, 3pt and FH) analysis, there is mild tension when including the current times $\tau = 1$ and $\tau = t_{\text{sep}} - 1$ for $t_{\text{sep}} > 10$ and so our optimal fit removes one extra current insertion time for these later t_{sep} values. For FH, the τ range indicates the values used in the summation over current time.

| | (2pt, 3pt) | (2pt, FH) | (2pt, 3pt, FH) |
|----------------------------|---------------------------|---------------------------|---|
| 2pt t_{sep} range | [3, 17] | [5, 17] | [3, 17] |
| 3pt t_{sep} range | [3, 14] | – | [3, 14] |
| FH t_{sep} range | – | [5, 13] | [3, 13] |
| 3pt τ range | $[1, t_{\text{sep}} - 1]$ | $[1, t_{\text{sep}} - 1]$ | $[1, t_{\text{sep}} - 1], t_{\text{sep}} \leq 10$ $[1, t_{\text{sep}} - 1], t_{\text{sep}} > 10$ |
| FH τ range | – | $[1, t_{\text{sep}} - 1]$ | $[1, t_{\text{sep}} - 1]$ |
| n_{states} | 5 | 2 | 5 |

- [1] S. Aoki *et al.* (Flavour Lattice Averaging Group), “FLAG Review 2019: Flavour Lattice Averaging Group (FLAG),” *Eur. Phys. J. C* **80**, 113 (2020), [arXiv:1902.08191 \[hep-lat\]](#).
- [2] G. Peter Lepage, “The Analysis of Algorithms for Lattice Field Theory,” in *TASI, Boulder* (1989) pp. 97–120, [https://inspirehep.net/literature/287173](#).
- [3] G. P. Lepage, B. Clark, C. T. H. Davies, K. Hornbostel, P. B. Mackenzie, C. Morningstar, and H. Trotter, “Constrained curve fitting,” *Nucl. Phys. B Proc. Suppl.* **106**, 12–20 (2002), [arXiv:hep-lat/0110175](#).
- [4] Matthew Wingate, Junko Shigemitsu, Christine T. H. Davies, G. Peter Lepage, and Howard D. Trotter, “Heavy light mesons with staggered light quarks,” *Phys. Rev. D* **67**, 054505 (2003), [arXiv:hep-lat/0211014](#).
- [5] Elvira Gamiz, Christine T. H. Davies, G. Peter Lepage, Junko Shigemitsu, and Matthew Wingate (HPQCD), “Neutral B Meson Mixing in Unquenched Lattice QCD,” *Phys. Rev. D* **80**, 014503 (2009), [arXiv:0902.1815 \[hep-lat\]](#).
- [6] A. Bazavov *et al.* (Fermilab Lattice, MILC), “ $B_{(s)}^0$ -mixing matrix elements from lattice QCD for the Standard Model and beyond,” *Phys. Rev. D* **93**, 113016 (2016), [arXiv:1602.03560 \[hep-lat\]](#).
- [7] A. Bazavov *et al.* (Fermilab Lattice, MILC), “ $|V_{us}|$ from $K_{\ell 3}$ decay and four-flavor lattice QCD,” *Phys. Rev. D* **99**, 114509 (2019), [arXiv:1809.02827 \[hep-lat\]](#).
- [8] R. G. Edwards, G. T. Fleming, Ph. Hagler, J. W. Negele, K. Orginos, A. V. Pochinsky, D. B. Renner, D. G. Richards, and W. Schroers (LHPC), “The Nucleon axial charge in full lattice QCD,” *Phys. Rev. Lett.* **96**, 052001 (2006), [arXiv:hep-lat/0510062](#).
- [9] Takeshi Yamazaki, Yasumichi Aoki, Tom Blum, Huey-Wen Lin, Shigemi Ohta, Shoichi Sasaki, Robert Tweedie, and James Zanotti, “Nucleon form factors with 2+1 flavor dynamical domain-wall fermions,” *Phys. Rev. D* **79**, 114505 (2009), [arXiv:0904.2039 \[hep-lat\]](#).
- [10] J. D. Bratt *et al.* (LHPC), “Nucleon structure from mixed action calculations using 2+1 flavors of asqtad sea and domain wall valence fermions,” *Phys. Rev. D* **82**, 094502 (2010), [arXiv:1001.3620 \[hep-lat\]](#).
- [11] C. Alexandrou, M. Brinet, J. Carbonell, M. Constantinou, P. A. Harraud, P. Guichon, K. Jansen, T. Korzec, and M. Papinutto (ETM), “Axial Nucleon form factors from lattice QCD,” *Phys. Rev. D* **83**, 045010 (2011), [arXiv:1012.0857 \[hep-lat\]](#).
- [12] R. L. Jaffe, “Delocalization of the axial charge in the chiral limit,” *Phys. Lett. B* **529**, 105–110 (2002), [arXiv:hep-ph/0108015](#).
- [13] Thomas D. Cohen, “The Extraction of $g(A)$ from finite volume systems: The Long and short of it,” *Phys. Lett. B* **529**, 50–56 (2002), [arXiv:hep-lat/0112014](#).
- [14] T. Yamazaki, Y. Aoki, T. Blum, H. W. Lin, M. F. Lin, S. Ohta, S. Sasaki, R. J. Tweedie, and J. M. Zanotti (RBC+UKQCD), “Nucleon axial charge in 2+1 flavor dynamical lattice QCD with domain wall fermions,” *Phys. Rev. Lett.* **100**, 171602 (2008), [arXiv:0801.4016 \[hep-lat\]](#).
- [15] Jeremy Green, John Negele, Andrew Pochinsky, Stefan Krieg, and Sergey Syritsyn, “Excited state contamination in nucleon structure calculations,” *PoS LATTICE2011*, 157 (2011), [arXiv:1111.0255 \[hep-lat\]](#).
- [16] Simon Dinter, Constantia Alexandrou, Martha Constantinou, Vincent Drach, Karl Jansen, and Dru B. Renner, “Precision Study of Excited State Effects in Nucleon Matrix Elements,” *Phys. Lett. B* **704**, 89–93 (2011), [arXiv:1108.1076 \[hep-lat\]](#).
- [17] S. Capitani, M. Della Morte, G. von Hippel, B. Jager, A. Jüttner, B. Knippschild, H. B. Meyer, and H. Wittig, “The nucleon axial charge from lattice QCD with controlled errors,” *Phys. Rev. D* **86**, 074502 (2012), [arXiv:1205.0180 \[hep-lat\]](#).
- [18] J. R. Green, M. Engelhardt, S. Krieg, J. W. Negele, A. V. Pochinsky, and S. N. Syritsyn, “Nucleon Structure from Lattice QCD Using a Nearly Physical Pion Mass,” *Phys. Lett. B* **734**, 290–295 (2014),

- arXiv:1209.1687 [hep-lat].
- [19] Tanmoy Bhattacharya, Saul D. Cohen, Rajan Gupta, Anosh Joseph, Huey-Wen Lin, and Boram Yoon, “Nucleon Charges and Electromagnetic Form Factors from 2+1+1-Flavor Lattice QCD,” *Phys. Rev. D* **89**, 094502 (2014), arXiv:1306.5435 [hep-lat].
- [20] G. S. Bali, S. Collins, B. Gläfle, M. Göckeler, J. Najjar, R. Rödl, A. Schäfer, R. Schiel, A. Sternbeck, and W. Söldner, “Moments of structure functions for $N_f = 2$ near the physical point,” *PoS LATTICE2013*, 290 (2014), arXiv:1311.7041 [hep-lat].
- [21] R. Horsley, Y. Nakamura, A. Nobile, P. E. L. Rakow, G. Schierholz, and J. M. Zanotti, “Nucleon axial charge and pion decay constant from two-flavor lattice QCD,” *Phys. Lett. B* **732**, 41–48 (2014), arXiv:1302.2233 [hep-lat].
- [22] Gunnar S. Bali, Sara Collins, Benjamin Glässle, Meinulf Göckeler, Johannes Najjar, Rudolf H. Rödl, Andreas Schäfer, Rainer W. Schiel, Wolfgang Söldner, and André Sternbeck, “Nucleon isovector couplings from $N_f = 2$ lattice QCD,” *Phys. Rev. D* **91**, 054501 (2015), arXiv:1412.7336 [hep-lat].
- [23] A. Abdel-Rehim *et al.*, “Nucleon and pion structure with lattice QCD simulations at physical value of the pion mass,” *Phys. Rev. D* **92**, 114513 (2015), [Erratum: *Phys.Rev.D* 93, 039904 (2016)], arXiv:1507.04936 [hep-lat].
- [24] Tanmoy Bhattacharya, Vincenzo Cirigliano, Saul Cohen, Rajan Gupta, Huey-Wen Lin, and Boram Yoon, “Axial, Scalar and Tensor Charges of the Nucleon from 2+1+1-flavor Lattice QCD,” *Phys. Rev. D* **94**, 054508 (2016), arXiv:1606.07049 [hep-lat].
- [25] Constantia Alexandrou, Martha Constantinou, Kyriakos Hadjiyiannakou, Karl Jansen, Christos Kallidonis, Giannis Koutsou, and Alejandro Vaquero Aviles-Casco, “Nucleon axial form factors using $N_f = 2$ twisted mass fermions with a physical value of the pion mass,” *Phys. Rev. D* **96**, 054507 (2017), arXiv:1705.03399 [hep-lat].
- [26] Stefano Capitani, Michele Della Morte, Dalibor Djukanovic, Georg M. von Hippel, Jiayu Hua, Benjamin Jäger, Parikshit M. Junnarkar, Harvey B. Meyer, Thomas D. Rae, and Hartmut Wittig, “Isovector axial form factors of the nucleon in two-flavor lattice QCD,” *Int. J. Mod. Phys. A* **34**, 1950009 (2019), arXiv:1705.06186 [hep-lat].
- [27] E. Berkowitz, C. Bouchard, D. B. Brantley, C.C Chang, M.A. Clark, N. Garron, B Joó, T. Kurth, C. Monahan, H. Monge-Camacho, A. Nicholson, K. Orginos, E. Rinaldi, P. Vranas, and A. Walker-Loud, “An accurate calculation of the nucleon axial charge with lattice QCD,” (2017), arXiv:1704.01114 [hep-lat].
- [28] C. C. Chang, A. Nicholson, E. Rinaldi, E. Berkowitz, N. Garron, D. A. Brantley, H. Monge-Camacho, C. J. Monahan, C. Bouchard, M. A. Clark, B. Joó, T. Kurth, K. Orginos, P. Vranas, and A. Walker-Loud, “A percent-level determination of the nucleon axial coupling from quantum chromodynamics,” *Nature* **558**, 91–94 (2018), arXiv:1805.12130 [hep-lat].
- [29] Evan Berkowitz, M. A. Clark, A. Gambhir, K. McElvain, A. Nicholson, E. Rinaldi, P. Vranas, A. Walker-Loud, C. C. Chang, B. Joó, T. Kurth, and K. Orginos, “Simulating the weak death of the neutron in a femtoscale universe with near-Exascale computing,” (2018), arXiv:1810.01609 [hep-lat].
- [30] André Walker-Loud *et al.*, “Lattice QCD Determination of g_A ,” *PoS CD2018*, 020 (2020), arXiv:1912.08321 [hep-lat].
- [31] Rajan Gupta, Yong-Chull Jang, Boram Yoon, Huey-Wen Lin, Vincenzo Cirigliano, and Tanmoy Bhattacharya, “Isovector Charges of the Nucleon from 2+1+1-flavor Lattice QCD,” *Phys. Rev. D* **98**, 034503 (2018), arXiv:1806.09006 [hep-lat].
- [32] Nesreen Hasan, Jeremy Green, Stefan Meinel, Michael Engelhardt, Stefan Krieg, John Negele, Andrew Pochinsky, and Sergey Syritsyn, “Nucleon axial, scalar, and tensor charges using lattice QCD at the physical pion mass,” *Phys. Rev. D* **99**, 114505 (2019), arXiv:1903.06487 [hep-lat].
- [33] C. Alexandrou, S. Bacchio, M. Constantinou, J. Finkenrath, K. Hadjiyiannakou, K. Jansen, G. Koutsou, and A. Vaquero Aviles-Casco, “Nucleon axial, tensor, and scalar charges and σ -terms in lattice QCD,” *Phys. Rev. D* **102**, 054517 (2020), arXiv:1909.00485 [hep-lat].
- [34] Sungwoo Park, Rajan Gupta, Boram Yoon, Santanu Mondal, Tanmoy Bhattacharya, Yong-Chull Jang, Bálint Joó, and Frank Winter (Nucleon Matrix Elements (NME)), “Precision Nucleon Charges and Form Factors Using 2+1-flavor Lattice QCD,” (2021), arXiv:2103.05599 [hep-lat].
- [35] P. A. Zyla *et al.* (Particle Data Group), “Review of Particle Physics,” *PTEP* **2020**, 083C01 (2020).
- [36] P. Bopp, D. Dubbers, L. Hornig, E. Klemt, J. Last, H. Schütze, S. J. Freedman, and O. Schärpf, “Beta-decay asymmetry of the neutron and $\frac{g_A}{g_V}$,” *Phys. Rev. Lett.* **56**, 919–922 (1986).
- [37] B. Yerozolimsky, I. Kuznetsov, Yu. Mostovoy, and I. Stepanenko, “Corrigendum: Corrected value of the beta-emission asymmetry in the decay of polarized neutrons measured in 1990,” *Physics Letters B* **412**, 240 – 241 (1997).
- [38] P. Liaud, K. Schreckenbach, R. Kossakowski, H. Nastoll, A. Bussière, J.P. Guillaud, and L. Beck, “The measurement of the beta asymmetry in the decay of polarized neutrons,” *Nuclear Physics A* **612**, 53 – 81 (1997).
- [39] Y. A. Mostovoi *et al.*, “Experimental value of $G(A)/G(V)$ from a measurement of both P-odd correlations in free-neutron decay,” *Phys. Atom. Nucl.* **64**, 1955–1960 (2001), [*Yad. Fiz.*64,2040(2001)].
- [40] M. Schumann, M. Kreuz, M. Deissenroth, F. Glück, J. Krempel, B. Märkisch, D. Mund, A. Petoukhov, T. Soldner, and H. Abele, “Measurement of the proton asymmetry parameter in neutron beta decay,” *Phys. Rev. Lett.* **100**, 151801 (2008).
- [41] D. Mund, B. Märkisch, M. Deissenroth, J. Krempel, M. Schumann, H. Abele, A. Petoukhov, and T. Soldner, “Determination of the Weak Axial Vector Coupling from a Measurement of the Beta-Asymmetry Parameter A in Neutron Beta Decay,” *Phys. Rev. Lett.* **110**, 172502 (2013), arXiv:1204.0013 [hep-ex].
- [42] M. P. Mendenhall *et al.* (UCNA), “Precision measurement of the neutron β -decay asymmetry,” *Phys. Rev. C* **87**, 032501 (2013), arXiv:1210.7048 [nucl-ex].
- [43] B. Märkisch *et al.*, “Measurement of the Weak Axial-Vector Coupling Constant in the Decay of Free Neutrons Using a Pulsed Cold Neutron Beam,” *Phys. Rev. Lett.* **122**, 242501 (2019), arXiv:1812.04666 [nucl-ex].

- [44] M. Beck *et al.*, “Improved determination of the β - $\bar{\nu}_e$ angular correlation coefficient a in free neutron decay with the *aSPECT* spectrometer,” *Phys. Rev. C* **101**, 055506 (2020), arXiv:1908.04785 [nucl-ex].
- [45] Chris Bouchard, Chia Cheng Chang, Thorsten Kurth, Kostas Orginos, and Andre Walker-Loud, “On the Feynman-Hellmann Theorem in Quantum Field Theory and the Calculation of Matrix Elements,” *Phys. Rev. D* **96**, 014504 (2017), arXiv:1612.06963 [hep-lat].
- [46] William Detmold, C. J. David Lin, and Stefan Meinel, “Axial couplings and strong decay widths of heavy hadrons,” *Phys. Rev. Lett.* **108**, 172003 (2012), arXiv:1109.2480 [hep-lat].
- [47] William Detmold, C. J. David Lin, and Stefan Meinel, “Calculation of the heavy-hadron axial couplings g_1 , g_2 and g_3 using lattice QCD,” *Phys. Rev. D* **85**, 114508 (2012), arXiv:1203.3378 [hep-lat].
- [48] E. Follana, Q. Mason, C. Davies, K. Hornbostel, G. P. Lepage, J. Shigemitsu, H. Trottier, and K. Wong (HPQCD, UKQCD), “Highly improved staggered quarks on the lattice, with applications to charm physics,” *Phys. Rev. D* **75**, 054502 (2007), arXiv:hep-lat/0610092.
- [49] A. Bazavov *et al.* (MILC), “Lattice QCD Ensembles with Four Flavors of Highly Improved Staggered Quarks,” *Phys. Rev. D* **87**, 054505 (2013), arXiv:1212.4768 [hep-lat].
- [50] Nolan Miller *et al.*, “ F_K/F_π from Möbius Domain-Wall fermions solved on gradient-flowed HISQ ensembles,” *Phys. Rev. D* **102**, 034507 (2020), arXiv:2005.04795 [hep-lat].
- [51] Nolan Miller *et al.*, “Scale setting the Möbius Domain Wall Fermion on gradient-flowed HISQ action using the omega baryon mass and the gradient-flow scales t_0 and w_0 ,” *Phys. Rev. D* **103**, 054511 (2021), arXiv:2011.12166 [hep-lat].
- [52] Richard C. Brower, Harmut Neff, and Kostas Orginos, “The Möbius domain wall fermion algorithm,” *Comput. Phys. Commun.* **220**, 1–19 (2017), arXiv:1206.5214 [hep-lat].
- [53] David B. Kaplan, “A Method for simulating chiral fermions on the lattice,” *Phys. Lett. B* **288**, 342–347 (1992), arXiv:hep-lat/9206013.
- [54] Yigal Shamir, “Chiral fermions from lattice boundaries,” *Nucl. Phys. B* **406**, 90–106 (1993), arXiv:hep-lat/9303005.
- [55] Vadim Furman and Yigal Shamir, “Axial symmetries in lattice QCD with Kaplan fermions,” *Nucl. Phys. B* **439**, 54–78 (1995), arXiv:hep-lat/9405004.
- [56] Evan Berkowitz *et al.*, “Möbius domain-wall fermions on gradient-flowed dynamical HISQ ensembles,” *Phys. Rev. D* **96**, 054513 (2017), arXiv:1701.07559 [hep-lat].
- [57] G. Peter Lepage and Paul B. Mackenzie, “On the viability of lattice perturbation theory,” *Phys. Rev. D* **48**, 2250–2264 (1993), arXiv:hep-lat/9209022.
- [58] André Walker-Loud, “CaLat elastic nucleon structure: I,” Lattice 2019, <https://indico.cern.ch/event/764552/contributions/3420541/>.
- [59] Yong-Chull Jang, Rajan Gupta, Boram Yoon, and Tanmoy Bhattacharya, “Axial Vector Form Factors from Lattice QCD that Satisfy the PCAC Relation,” *Phys. Rev. Lett.* **124**, 072002 (2020), arXiv:1905.06470 [hep-lat].
- [60] L. Maiani, G. Martinelli, M. L. Paciello, and B. Taglienti, “Scalar Densities and Baryon Mass Differences in Lattice {QCD} With Wilson Fermions,” *Nucl. Phys. B* **293**, 420 (1987).
- [61] Konstantin Ottnad, “Excited states in nucleon structure calculations,” in *38th International Symposium on Lattice Field Theory* (2020) arXiv:2011.12471 [hep-lat].
- [62] Brian C. Tiburzi, “Time Dependence of Nucleon Correlation Functions in Chiral Perturbation Theory,” *Phys. Rev. D* **80**, 014002 (2009), arXiv:0901.0657 [hep-lat].
- [63] Oliver Bär and Maarten Golterman, “Excited-state contribution to the axial-vector and pseudoscalar correlators with two extra pions,” *Phys. Rev. D* **87**, 014505 (2013), arXiv:1209.2258 [hep-lat].
- [64] Oliver Bar, “Nucleon-pion-state contribution to nucleon two-point correlation functions,” *Phys. Rev. D* **92**, 074504 (2015), arXiv:1503.03649 [hep-lat].
- [65] Brian C. Tiburzi, “Chiral Corrections to Nucleon Two- and Three-Point Correlation Functions,” *Phys. Rev. D* **91**, 094510 (2015), arXiv:1503.06329 [hep-lat].
- [66] Oliver Bär, “Nucleon-pion-state contribution in lattice calculations of the nucleon charges g_A , g_T and g_S ,” *Phys. Rev. D* **94**, 054505 (2016), arXiv:1606.09385 [hep-lat].
- [67] Oliver Bar, “Chiral perturbation theory and nucleon-pion-state contaminations in lattice QCD,” *Int. J. Mod. Phys. A* **32**, 1730011 (2017), arXiv:1705.02806 [hep-lat].
- [68] Gunnar S. Bali, Lorenzo Barca, Sara Collins, Michael Gruber, Marius Löffler, Andreas Schäfer, Wolfgang Söldner, Philipp Wein, Simon Weishäupl, and Thomas Wurm (RQCD), “Nucleon axial structure from lattice QCD,” *JHEP* **05**, 126 (2020), arXiv:1911.13150 [hep-lat].
- [69] Oliver Bar, “ $N\pi$ states and the projection method for the nucleon axial and pseudoscalar form factors,” *Phys. Rev. D* **101**, 034515 (2020), arXiv:1912.05873 [hep-lat].
- [70] A. Walker-Loud *et al.*, “Light hadron spectroscopy using domain wall valence quarks on an Asqtad sea,” *Phys. Rev. D* **79**, 054502 (2009), arXiv:0806.4549 [hep-lat].
- [71] Andre Walker-Loud, “New lessons from the nucleon mass, lattice QCD and heavy baryon chiral perturbation theory,” *PoS LATTICE2008*, 005 (2008), arXiv:0810.0663 [hep-lat].
- [72] André Walker-Loud, “Baryons in/and Lattice QCD,” *PoS CD12*, 017 (2013), arXiv:1304.6341 [hep-lat].
- [73] André Walker-Loud, “Nuclear Physics Review,” *PoS LATTICE2013*, 013 (2014), arXiv:1401.8259 [hep-lat].
- [74] Christian Drischler, Wick Haxton, Kenneth McElvain, Emanuele Mereghetti, Amy Nicholson, Pavlos Vranas, and André Walker-Loud, “Towards grounding nuclear physics in QCD,” (2019), arXiv:1910.07961 [nucl-th].
- [75] Ben Hörz *et al.*, “Two-nucleon S-wave interactions at the $SU(3)$ flavor-symmetric point with $m_{ud} \simeq m_s^{\text{phys}}$: A first lattice QCD calculation with the stochastic Laplacian Heaviside method,” *Phys. Rev. C* **103**, 014003 (2021), arXiv:2009.11825 [hep-lat].
- [76] Boram Yoon *et al.*, “Isovector charges of the nucleon from 2+1-flavor QCD with clover fermions,” *Phys. Rev. D* **95**, 074508 (2017), arXiv:1611.07452 [hep-lat].
- [77] Rajan Gupta, Yong-Chull Jang, Huey-Wen Lin, Boram Yoon, and Tanmoy Bhattacharya, “Axial Vector Form Factors of the Nucleon from Lattice QCD,” *Phys. Rev. D* **96**, 114503 (2017), arXiv:1705.06834 [hep-lat].

- [78] S. Gusken, U. Low, K. H. Mutter, R. Sommer, A. Patel, and K. Schilling, “Nonsinglet Axial Vector Couplings of the Baryon Octet in Lattice {QCD},” *Phys. Lett. B* **227**, 266–269 (1989).
- [79] John Bulava, Michael Donnellan, and Rainer Sommer, “On the computation of hadron-to-hadron transition matrix elements in lattice QCD,” *JHEP* **01**, 140 (2012), [arXiv:1108.3774 \[hep-lat\]](#).
- [80] G. M. de Divitiis, R. Petronzio, and N. Tantalo, “On the extraction of zero momentum form factors on the lattice,” *Phys. Lett. B* **718**, 589–596 (2012), [arXiv:1208.5914 \[hep-lat\]](#).
- [81] A. J. Chambers *et al.* (CSSM, QCDSF/UKQCD), “Feynman-Hellmann approach to the spin structure of hadrons,” *Phys. Rev. D* **90**, 014510 (2014), [arXiv:1405.3019 \[hep-lat\]](#).
- [82] A. J. Chambers *et al.*, “Disconnected contributions to the spin of the nucleon,” *Phys. Rev. D* **92**, 114517 (2015), [arXiv:1508.06856 \[hep-lat\]](#).
- [83] Martin J. Savage, Phiala E. Shanahan, Brian C. Tiburzi, Michael L. Wagman, Frank Winter, Silas R. Beane, Emmanuel Chang, Zohreh Davoudi, William Detmold, and Kostas Orginos, “Proton-Proton Fusion and Tritium β Decay from Lattice Quantum Chromodynamics,” *Phys. Rev. Lett.* **119**, 062002 (2017), [arXiv:1610.04545 \[hep-lat\]](#).
- [84] Robert G. Edwards and Balint Joo (SciDAC, LHPC, UKQCD), “The Chroma software system for lattice QCD,” *Nucl. Phys. B Proc. Suppl.* **140**, 832 (2005), [arXiv:hep-lat/0409003](#).
- [85] S. Basak, R. G. Edwards, G. T. Fleming, U. M. Heller, C. Morningstar, D. Richards, I. Sato, and S. Wallace, “Group-theoretical construction of extended baryon operators in lattice QCD,” *Phys. Rev. D* **72**, 094506 (2005), [arXiv:hep-lat/0506029](#).
- [86] Subhasish Basak, Robert Edwards, George T. Fleming, Urs M. Heller, Colin Morningstar, David Richards, Ikuro Sato, and Stephen J. Wallace (Lattice Hadron Physics (LHPC)), “Clebsch-Gordan construction of lattice interpolating fields for excited baryons,” *Phys. Rev. D* **72**, 074501 (2005), [arXiv:hep-lat/0508018](#).
- [87] Jozef J. Dudek, Robert G. Edwards, and Christopher E. Thomas (Hadron Spectrum), “Energy dependence of the ρ resonance in $\pi\pi$ elastic scattering from lattice QCD,” *Phys. Rev. D* **87**, 034505 (2013), [Erratum: *Phys.Rev.D* 90, 099902 (2014)], [arXiv:1212.0830 \[hep-ph\]](#).
- [88] C. B. Lang and V. Verduci, “Scattering in the πN negative parity channel in lattice QCD,” *Phys. Rev. D* **87**, 054502 (2013), [arXiv:1212.5055 \[hep-lat\]](#).
- [89] David J. Wilson, Raul A. Briceño, Jozef J. Dudek, Robert G. Edwards, and Christopher E. Thomas, “Coupled $\pi\pi, K\bar{K}$ scattering in P -wave and the ρ resonance from lattice QCD,” *Phys. Rev. D* **92**, 094502 (2015), [arXiv:1507.02599 \[hep-ph\]](#).
- [90] Raúl A. Briceño, Maxwell T. Hansen, and Andrew W. Jackura, “Consistency checks for two-body finite-volume matrix elements: I. Conserved currents and bound states,” *Phys. Rev. D* **100**, 114505 (2019), [arXiv:1909.10357 \[hep-lat\]](#).
- [91] “LALIBE: CalLat Collaboration code for lattice qcd calculations,” <https://github.com/callat-qcd/lalibe>.
- [92] M.A. Clark, R. Babich, K. Barros, R.C. Brower, and C. Rebbi, “Solving Lattice QCD systems of equations using mixed precision solvers on GPUs,” *Comput.Phys.Commun.* **181**, 1517–1528 (2010), <https://github.com/lattice/quda>, [arXiv:0911.3191 \[hep-lat\]](#).
- [93] R. Babich, M.A. Clark, B. Joo, G. Shi, R.C. Brower, *et al.*, “Scaling Lattice QCD beyond 100 GPUs,” (2011), [arXiv:1109.2935 \[hep-lat\]](#).
- [94] The HDF Group, “Hierarchical Data Format, version 5,” (1997-NNNN), <http://www.hdfgroup.org/HDF5/>.
- [95] Thorsten Kurth, Andrew Pochinsky, Abhinav Sarje, Sergey Syritsyn, and Andre Walker-Loud, “High-Performance I/O: HDF5 for Lattice QCD,” *Proceedings, 32nd International Symposium on Lattice Field Theory (Lattice 2014): Brookhaven, NY, USA, June 23-28, 2014*, PoS **LATTICE2014**, 045 (2015), [arXiv:1501.06992 \[hep-lat\]](#).
- [96] Evan Berkowitz, “METAQ: Bundle Supercomputing Tasks,” (2017), <https://github.com/evanberkowitz/metaq>, [arXiv:1702.06122 \[physics.comp-ph\]](#).
- [97] Evan Berkowitz, Gustav R. Jansen, Kenneth McElvain, and André Walker-Loud, “Job Management and Task Bundling,” *EPJ Web Conf.* **175**, 09007 (2018), [arXiv:1710.01986 \[hep-lat\]](#).
- [98] Chia Cheng Chang, Christopher Körber, and André Walker-Loud, “EspressoDB: A Scientific Database for Managing High-Performance Computing Workflow,” *J. Open Source Softw.* **5**, 2007 (2020), [arXiv:1912.03580 \[hep-lat\]](#).
- [99] Peter Lepage, “gvar,” (2020), <https://github.com/gplepage/gvar>.
- [100] Peter Lepage, “lsqfit,” (2021), <https://github.com/gplepage/lsqfit>.
- [101] Evan Berkowitz *et al.*, “Progress in Multibaryon Spectroscopy,” *PoS LATTICE2018*, 003 (2018), [arXiv:1902.09416 \[hep-lat\]](#).